The University of Queensland
School of Mathematics and Physics

More from Less
High efficiency low donor content organic solar cells

Honours Thesis of
Shaun McAnally

Supervisors
Prof. Paul Burn
Dr Paul Shaw

November 2021

Statement of Authenticity

This is to certify that to the best of my knowledge, the content of this thesis is my own work. This thesis has not been submitted for any degree or other purposes. I certify that the intellectual content of this thesis is the product of my own work and that all the assistance received in preparing this thesis and sources have been acknowledged.

SHAUN MCANALLY

Abstract

Organic photovoltaic devices (OPVs) will play a role in the future energy mix as we endeavour to globally transition to renewable sources of electricity. The application of organic semiconducting materials enable the fabrication of lightweight, flexible photovoltaic devices with a simple fabrication process that has a significantly reduced energy investment when compared with silicon-based photovoltaics. The most efficient OPV devices have a blend of electron donor and acceptor materials that constitute the light absorbing layer, known as a bulk heterojunction. A particularly active area of research in OPVs has been the development of small molecule acceptors. When paired with a suitable polymer donor in an appropriate ratio, power conversion efficiencies of up to 18.2% can be achieved. For many donor-acceptor blends, the weight ratio of donor to acceptor are often near equal. This equal weight ratio is seen as a way of ensuring the formation of a continuous interpenetrating network of donor and acceptor molecules to facilitate efficient dissociation of electron-hole pairs (excitons) and subsequent charge transport. Controlling the film morphology is critical but not always simple to achieve in a reliable way, particularly at scale. However, minimising the quantity of polymer donor used in the fabrication of OPV devices is a pathway towards more consistent large-area device manufacturing. This research programme investigates the performance of two of the best performing acceptor materials in low donor content OPV devices. The optical properties and bulk morphology of the neat materials and blends containing them were investigated and compared. Finally, it is shown that, even when the donor polymer content was as low as $\sim 11\%$, the overall device performance was comparable to that of the optimised one-to-one by weight blend ratios.

Acknowledgements

I would like to thank my supervisors, Dr Paul Shaw and Prof. Paul Burn, for their continual guidance and support throughout this project. The insights they provided along the way gave context to the broader picture of my work and our discussions always left me feeling inspired and ready to start on the next step. They cultivated my passion to understand the various facets of this field more deeply and provided the resources to allow me to explore.

To the team at COPE, I am grateful for having the opportunity to join such an inclusive and dynamic research family. Conversations in the office about our various projects would regularly be the highlight of my day and it was inspiring to work with such a driven team. In one way or another, every member of the team contributed to my understanding of the various concepts and techniques that I developed along the way. In particular, I would like to thank Dr Hellen Jin for her guidance in planning and conducting my work at our facilities and Ronan Chu for providing morphology data that was critical to my project. I would also like to thank Dr Jeff Yun Huang and Dr Wael Al Abdulla from ANFF-Q for their advice and guidance on the fabrication and analysis tools relevant to my project.

Finally, I would like to acknowledge the support and patience of my parents Anne and Bruce, along with my family and close friends. Thank you for your constant encouragement and for being there to listen when I needed it most. I am deeply indebted to all of these wonderful people.

<div align="right">

Shaun McAnally
Brisbane
November 2021

</div>

Contents

Posing an existential risk to humanity, our rapidly deteriorating climate is the most time-critical societal issue of this century. Slowing the rate of anthropogenic global heating and irreversible environmental destruction will require a fundamental reshaping of the ways in which society views deeply ingrained habits of material consumption and energy use. The faster we, as a global community, are able to address the unsustainable aspects of our current consumption habits, the more effectively we will be able to avoid impending social and environmental disasters. If we break this enormous, interconnected issue down into streams based on the proportion of global greenhouse emissions a particular activity produces, our energy sector immediately takes centre stage. As of 2020, 57% of anthropogenic greenhouse gas emissions are produced by our energy usage, which is still driven in large part by the consumption of non-renewable fuel sources (Table 1.1).[1]

Table 1.1: Proportion of greenhouse gas emissions for each economic sector.[2]

Energy	57.0%
Agriculture & Land Use	18.4%
Transport	16.2%
Industrial Processes	5.2%
Waste	3.2%

Promoted as the two fundamental solutions to this energy dilemma are the complete electrification of the global economy and a transition of all energy generation to solely renewable sources. Both streams have an array of mature technological or policy-based solutions. Our challenge now is to develop technologies that can be implemented in scenarios with specific economic or environmental barriers where existing solutions are unfeasible. In terms of energy generation, this involves the development of novel technologies that suit the needs of people in developing countries or in regions where current renewable energy systems are too cumbersome to install at a useful energy density. Solving these (and other) implementation challenges are necessary to achieve true carbon neutrality in the energy sector. Continued research into novel forms of renewable energy generation is central to progress in this field, with emerging technologies in established fields providing some of the most promising solutions.

As of 2019, solar is the third largest source of renewable energy by installed capacity and currently the fastest growing energy source globally (Table 1.2).[2] Australia has the highest per capita energy

consumption from solar (1764 kWh per person) while the United States has the largest installed capacity at 62 gigawatts (Table 1.2).[2]

Table 1.2: Proportion of energy supply from renewable sources in 2020.[2]

Source	Proportion (2020)	Output (TWh) (1965)	Output (TWh) (2020)
Hydro	58%	1979.77	4355.04
Wind	21%	0	1590.19
Solar	12%	0	844.39
Other	9%	77.79	702.89

Crystalline silicon (c-Si) *photovoltaic* (PV), currently the dominant source of solar energy by installed capacity, has a number of significant challenges at each stage of the product lifecycle.

1. The high embedded energy (the work associated with manufacturing a product) of c-Si PV panels (as with all advanced consumer electronics) begins with the energy intensive refinement of raw materials.[3] Depending on the rate of energy production for a given c-Si PV device, conservative estimates of embedded energy indicate that it can take up to four years of solar energy production to offset for this initial energy investment.[4]

2. While we have witnessed a rapid decline in the price of c-Si PV devices for home and commercial installation, economies of scale can only go so far in reducing the cost of a technology that is inherently difficult to produce and resource intensive. The costs associated with their installation impose a significant economic barrier to entry for many, especially in developing countries where decentralised grids relying on modular and demand-based energy production would greatly benefit from the large-scale implementation of PV technology.[5]

3. c-Si PV panels are rigid and quite heavy ($\sim$18 kg/panel) and so they cannot be installed on curved or non-load-bearing surfaces.[6] The engineering restrictions imposed by c-Si PV limit their potential uses beyond rooftops and large-scale installations in population-sparse regions.

4. At the end of the device lifetime, the reclamation of rare earth elements in c-Si PV panels is another growing burden on global technology recycling infrastructure. As has been the case with consumer technology waste, it must not be made the responsibility of developing nations to deal with waste from renewable energy projects based (in large part) in developed regions.

Emerging PV technologies present new use cases that resolve many of these lifecycle challenges and, in doing so, expand the appeal of PV technology as an even more significant part of our renewables-led future.

Of the presently emerging PV solutions, *organic photovoltaic* (OPV) devices present a gamut of promising solutions to technical challenges faced by current-generation PV. As described in the following chapter, it is possible to foresee a future where commercialised OPV devices are cheap, rapidly printed on rigid or flexible substrates, semi-transparent and have a minimal lifecycle environmental impact. Taking the perspective of embedded energy, OPV devices reduce the cost recovery period from four years of energy generation for inorganic solar technology to just half a year.[3] Achieving this goal of readily available and transformative PV technology requires continued research into fundamental topics such as charge dynamics and materials synthesis to developing more efficient and reliable device manufacturing techniques.

This research project is a study of how OPV device performance is affected by altering the composition of the photoactive layer (the organic layer responsible for the generation of charge in an OPV device). Further investigation using a selection of analysis techniques, including ellipsometry and charge transport measurements, provide insight into the underlying reasons for associated changes in device performance. Understanding how we can modify the composition of the photoactive layer to simplify the device fabrication process while preserving the high efficiency of leading OPV materials will provide a pathway towards the use of these materials in large-scale device fabrication.

An Introduction to Organic Photovoltaics: The working principles

Permeating many areas of optoelectronics, organic semiconductor materials research has demonstrated promising paths towards more versatile, cheaper and environmentally friendly solutions to current technological challenges. The hallmark advantages of organic semiconductors - solution- or low temperature vacuum-processability, lightweight devices and mechanical flexibility have led to their use in a wide variety of commercial applications.[7] A now ubiquitous implementation of organic semiconductor technology, *organic light emitting diode* (OLED) displays have enabled completely new classes of technology, including advanced smartwatches that rely on energy efficient components and mobile device displays that have better colour reproduction than most reference monitors from just a decade ago (Figure 2.1). Other applications of organic semiconducting materials, including organic transistors, sensors and photodetectors and lasers, have undergone significant research in recent decades, with many technical solutions nearing a marketable state.

Aside from widely available OLED technology, a large and promising area of organic semiconductor research is now OPV devices. Although there is an established research community working on devices that are now close to matching the performance of inorganic photovoltaics in the lab and companies working to commercialise this technology, a number of key issues remain to be resolved. Commercially available OPV devices rely on older, more thoroughly investigated materials, however the next wave of advanced materials, using small molecules known as non-fullerene acceptors (NFAs) are expected to soon be ready for large-scale commercial production.[8–11] At present, the focus of a significant portion of OPV research investment is in the optimisation of device efficiency to bring leading materials closer in key performance metrics to the benchmark inorganic photovoltaic devices along with enhanced photostability to ensure device longevity.

One can foresee a near-term future where OPV devices fabricated using inexpensive, lightweight and environmentally friendly materials are readily available and transformative in the space of low cost renewable energy solutions. As a result of their lightness, mechanical flexibility and simple manufacturing process, OPV devices could be used in applications as diverse as providing power for developing regions to powering the next generation of *internet-of-things* (IoT) devices and microelectronics.[12] The ability to engineer a range of device characteristics on the molecular level also means that OPV devices can be used in applications not suited to other PV technology. Examples include indoor applications where the light absorption characteristics of the photoactive molecules can be tuned to the indoor light

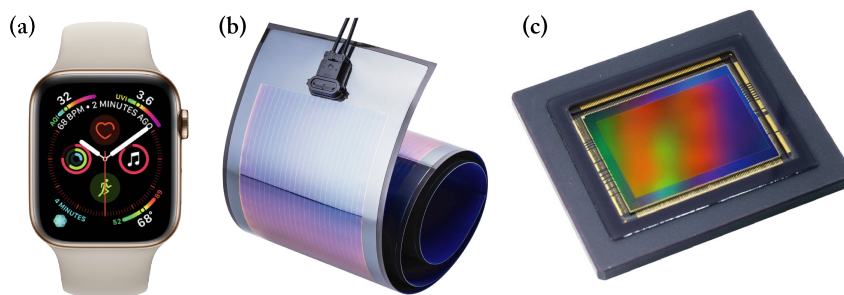spectra and in bio-safe devices[a]. [14,15]

FIGURE 2.1: Organic semiconducting materials have enabled completely new product categories as a result of their unique physical characteristics. (a) The low power consumption of OLED displays was central to the development of the original Apple Watch (Series 4 shown above). (b) Heliatek has had the greatest success in the scale-production of their flexible OPV devices using vacuum deposited small molecule materials. (c) Organic CMOS image sensors, such as this example by Canon, have higher dynamic range, a wider incident angle range and better protection from ambient humidity than conventional CMOS technology.

2.1 Organic Semiconductors

Taking a broad perspective, organic compounds are molecules that include covalently bonded carbon atoms.[16] While most organic solids exhibit insulating properties, some specific materials (those that are conjugated) are capable of carrying and transporting charges. Electronic processes in organic solids are complex as they bring together an array of physical phenomena, from intramolecular electronic structures to molecular interactions and charge-photon coupling to charge-charge coupling.

Excitations in a conjugated organic semiconductor occur due to the absorption of an incident photon, leading to a redistribution of electron density and a change in conformation.[17] The energy levels that control the light absorption and the charge carrier characteristics are the *highest occupied molecular orbital* (HOMO) and the *lowest unoccupied molecular orbital* (LUMO) levels.[18] The former defines the energy level of the molecule in the ground state while the latter defines the minimum energy required for an electron-hole pair (exciton) to be established in an organic semiconductor; in other words, the lowest energy excited state.[17] Both HOMO and LUMO levels are defined with respect to the ground state of a molecule since the ground state is a singlet state (Figure 2.2).[19]

Promotion of an electron to the LUMO (or higher) energy level occurs when a photon with energy greater than or equal to the HOMO-LUMO gap is absorbed.[18] The original singlet spin state is typically conserved in this process resulting in a singlet excited state, denoted S_1. The excited state of an organic semiconductor is known as an exciton[b]. The smallest HOMO-LUMO gap is therefore a result of the π-π^* transitions (where * denotes the antibonding state of the LUMO).[19] Many organic semiconductors are strongly coloured because the transition energy fortuitously lies in the visible spectrum (typically in the range of 1.5-3 eV). Changing the functional groups and physical properties of the core conjugation system results in changes to the observed optoelectronic materials of a given organic semiconductor. For instance, the length of the conjugation system is (approximately) inversely proportional to the magnitude of the energy gap.[19]

---

[a]OPV materials can be selected that are both suitable for contact with the human body and flexible.[13]

[b]π-conjugated organic molecules will also exhibit far stronger σ-bonds from the core structure of the molecule. Conjugation involves the overlap of p-orbitals to bridge alternating single bonds
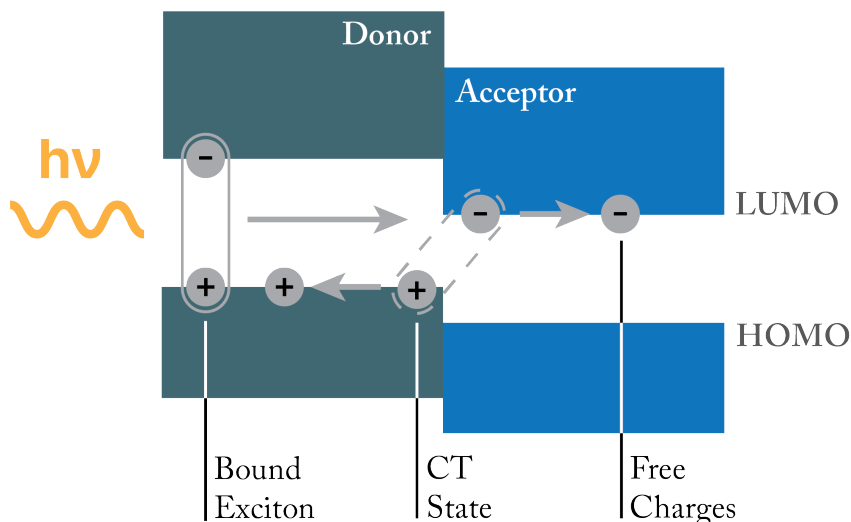
FIGURE 2.2: Excitons form as a result of the photoexcitation of a donor material with the electron in the LUMO level and hole in the HOMO level. These excitons diffuse to an interface between donor and acceptor materials with a HOMO-LUMO band offset. This energy offset facilitates the formation of a CT-state at the interface before the electron and hole separate into the different phases. Excitons can be formed in either the donor or acceptor materials, with either photoinduced electron or hole transfer occurring, respectively, to form the free charge carriers.

2.1.1 Organic Small Molecules

In the context of organic semiconducting materials, the small molecules label is typically applied to systems with a molecular weight on the order of $<10^3$ g·mol^{-1}. In terms of chemical synthesis, small molecule materials have the distinct advantage over conjugated polymers of being highly reproducible with good batch-to-batch consistency.[20]

Two classes of small molecule acceptors exist in OPV research: fullerenes and (the far larger family of) non-fullerenes (Figure 2.3). The key distinction is that, while fullerene materials have at their core a closed (or partially closed) carbon mesh, non-fullerene OPV materials can take any other form. While fullerene materials spurred the initial period of growth in the OPV field, the consensus is that this class of materials have reached peak performance with a record *power conversion efficiency* (PCE) of 12.1%.[21] In the framework of inorganic semiconductors, we can consider fullerene and non-fullerene materials to be n-type materials while the donors (often polymers) they are paired with act as p-type materials. A key distinction with non-fullerene materials is that the offsets between HOMO/LUMO levels can be tuned such that both acceptor and donor materials contribute to the generation of excitons.

2.1.2 Organic Macromolecules and Conjugated Polymers

Organic semiconducting macromolecules (oligomers) and conjugated polymers typically consist of chains of approximately ten or more repetitions of a given bonding unit (Figure 2.3).[16] When designing organic semiconducting polymers, the unit symmetry, backbone structure and the delocalisation of the π-electrons along this backbone need to be considered.[22] In the case of short oligomers (<10 monomer units), the length of the backbone chain can lead to significant changes in the HOMO-LUMO gap which can result in variability in overall device performance.[16] Due to the inherent uncertainty in conjugated polymer length, we consider the optical properties of a given polymer to lie

within a probabilistic distribution.

Organic small molecules were the first to be used in OPV devices as they could be vacuum deposited into polycrystalline layers while conjugated polymers necessitated the use of solution processing techniques.[23,24] Early OPV devices used vacuum deposited organic semiconductor materials to form the active layer. This process, however, has inherent disadvantages including significantly restricting the palette of materials that can be used to fabricate thin films. As the range of suitable organic semiconductor materials began to grow, solution processed OPV devices began to take precedence due to the possibility of low embedded energy manufacturing.
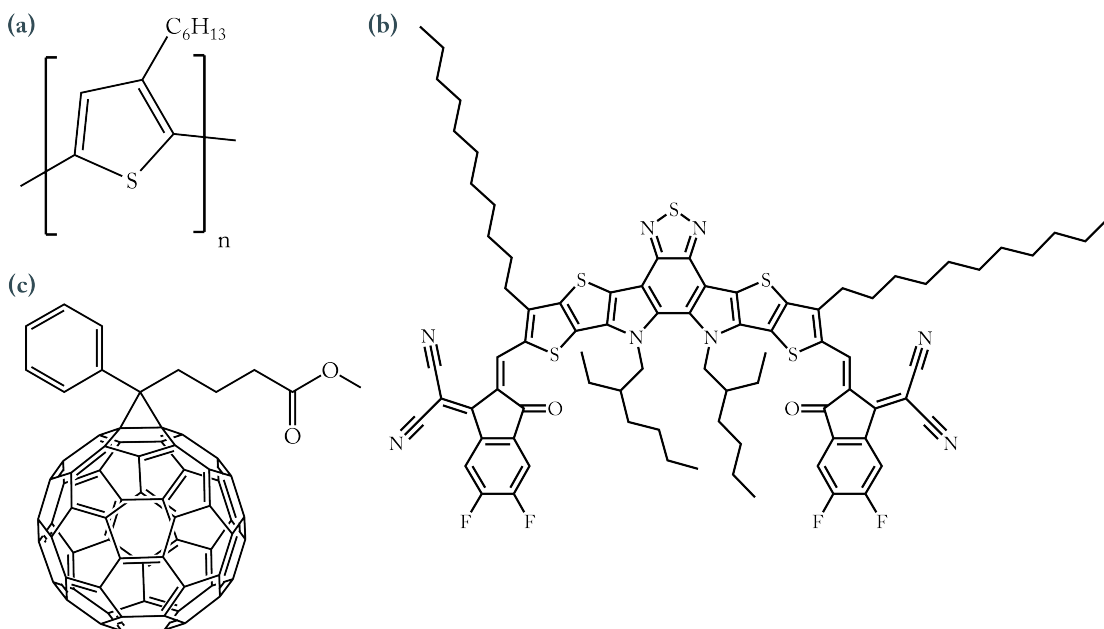

Figure 2.3: (a) P3HT is one of the most popular early polymer donor materials that forms nanofibrils in films, facilitating good exciton transfer even with low donor content in the donor-acceptor blend. (b) The Y6 family (discussed in greater detail in Section 3.2.2) is the best performing family of NFA small molecule materials synthesised thus far. (c) $PC_{61}BM$ is an established fullerene-based acceptor material that was typically paired with P3HT and other donor (both polymer and small molecule) materials in a BHJ.

2.2 Organic Photovoltaic Devices

In contrast with the highly ordered crystalline structures that make up inorganic semiconducting materials, organic thin-films are at best semicrystalline. As a result of the local changes in polarisation energy that occur due to this high degree of disorder, energetic band structures are not formed and we instead observe a Gaussian distribution consisting of the energy levels each constituent molecule.[17] Following photoexcitation, one of the two electrons filling the HOMO level in a conjugated system will be promoted to the LUMO level, forming an exciton. In a heterojunction-containing device, the exciton then migrates to a donor-acceptor interface where it separates into free charges that are then extracted from the device[c].

---

[c]If the incident photon is of a high enough energy, the molecule may transition from S_0 to S_n where n>1. When this transition does occur, the molecule will quickly decay to the S_1 state in a process known as internal interconversion which occurs in less than 10^{-12} seconds.[19]

2.2.1 Device structure

The fundamental structure of an OPV device includes an active layer (typically a donor-acceptor thin film blend) sandwiched between two conductive layers (i.e., the cathode and anode) that have been paired with suitable electron and hole transport layers (Figure 4.6). The active layer is composed of organic semiconducting materials that, via the processes described above, generate charges that can be collected by the cathode and anode that result in a photocurrent generated by the OPV device. In the pursuit of high performance and increased device longevity, OPV device research will usually involve trialling a range of parameters from active layer thickness to material blend ratios. Once the organic semiconducting materials have been synthesised, it is necessary to use the measured physical properties of the active materials to select appropriate device parameters that will facilitate optimised photon absorption and charge extraction. The main factors that influence the performance of the active layer are:

Energy level matching to ensure that the HOMO-LUMO gap of the materials of an active layer form an energetic cascade that facilitates efficient electron and hole collection at the electrodes, improving overall device performance by minimising CT-state losses. Small optical gap organic semiconducting materials are advantageous as they can absorb longer wavelength (near-infrared) light, which is the dominant component of spectral irradiance from the Sun.[17]

Bulk morphology balancing maximised light absorption with charge generation and extraction. Blended junctions can enable an increased active layer thickness for better light absorption while maintaining strong charge transport properties by maximising interfacial area between donor and acceptor phases.

Photon absorption that is strong in the visible and near-infrared regions (the wavelength range of light incident from the sun) from each material in the active layer. The complementary absorption spectra of donor and acceptor materials can also widen the wavelength range that is efficiently absorbed by the device. Organic thin films used for OPV devices are a thousandth of the thickness required for inorganic photovoltaic applications as OPV materials absorb light more effectively than their inorganic counterparts, especially at longer wavelengths. This longer-wavelength radiation makes up a significant proportion of the solar spectrum.

Charge mobility after exciton dissociation must be maximised so as to avoid losses due to electron-hole recombination. Phase separation in the active BHJ layer through the formation of amorphous aggregates, colloidal crystal structures and fibrils can enhance the charge transport characteristics of the thin film and reduce the rate of charge recombination.

2.2.2 Optimising exciton generation and diffusion

Excitons generated in the photoexcitation of π-conjugated molecules can transfer to a neighbouring molecule as a result of intermolecular electrostatic and electron-exchange potentials. Exciton transfer for singlet excited states occurs predominantly though long-range resonant dipole-dipole interactions between donor and acceptor pairs, which we can describe with the theoretical framework of *Fluorescence Resonant Energy Transfer* (FRET). In the case of organic semiconductor materials, we consider chromophores as dipole oscillators capable of exchanging energy as long as they have similar resonant frequencies (i.e., HOMO-LUMO gap energies). With this overlap of emission spectrum of the donor and absorption spectrum of the acceptor, we can define the FRET radius (R_0) as the rate
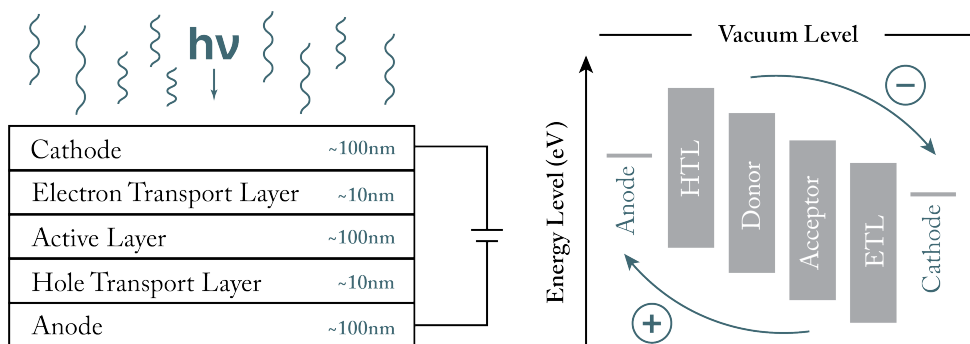
FIGURE 2.4: (a) The conventional structure of an OPV device with standard layer thicknesses. The active layer is the organic semiconductor BHJ, while the electron and hole transport layers (ETL and HTL, respectively) facilitate charge collection and transfer to the metallic electrodes. (b) The idealised energy bandgap cascade for each layer of a conventional structure OPV device. Each material has been selected so as to avoid energy losses due to charge recombination.

constant of energy transfer (D→A) and we can express this as,

$$k_{DA} = \frac{1}{\tau_D} \left(\frac{R_0}{R} \right)^6,$$ (2.1)

where τ_D represents the donor fluorescence lifetime and R the distance between the donor-acceptor pair. Using this relationship, the FRET radius gives us the distance at which FRET efficiency for exciton diffusion to the donor-acceptor interface is 50%. For some donor-acceptor pairs, the FRET radius can be on the order of 1 to 10 nm, at least an order of magnitude larger than the molecule size. This relationship helps us to understand how the intermolecular interactions in a thin-film can result in energy transfer to the donor-acceptor interfaces in the active layer thin-films described in subsection 2.2.2.

2.2.3   Maximising exciton dissociation and free charge generation

When an exciton reaches an interfacial region between donor and acceptor molecule, the energetic offset of HOMO and LUMO levels provides the driving force that facilitates the exciton dissociation. In the intermediary CT state, the hole and electron of the exciton pair will reside on the adjacent donor and acceptor molecules.[16] From this bound CT state, the hole and electron pair need to dissociate with high efficiency such that recombination of hole and electron is avoided. Dissociation of the coulomb-bound charge pairs into free charges occurs predominantly due to the motion of electrons on the picosecond timescale.[25] The CT state dissociation efficiency is seen as the major restricting factor in the generation rate of free charge carriers.[26]

Originally, OPV devices were fabricated with a single active layer material which placed limits on the rate of exciton dissociation as the thermal energy of the system at room temperature was not sufficient to overcome the exciton binding energy.[27,28] Bilayer heterojunction devices have the distinct advantage over homojunction devices of providing a cascading energetic pathway that facilitates a higher rate of exciton dissociation and subsequent charge extraction.[28] The issue with this approach, however, is that increasing the thickness of the donor and acceptor layers to increase photoabsorption results in regions where light is absorbed but no photocurrent is generated due to the very small length-scale of exciton diffusion meaning that many excitons do not reach the interface for charge generation. The best method of resolving the issue of limited interfacial surface area is to blend the

donor and acceptor materials together to form a BHJ. This approach is advantageous as instead of a single interface between the donor and acceptor phases, the BHJ has an immensely large interfacial surface area throughout the bulk of the film, facilitating a greater rate of exciton dissociation and energy transfer through the bulk. The BHJ acts, in this case, as a p-n junction with the electric field across the boundary of the donor and acceptor materials. [29,30] The rate of exciton dissociation at interfaces to free charge carriers within the BHJ depends most significantly on the average domain size of the materials within the active layer. [31,32] Once excitons dissociate at the interface, one must also consider the process of charge transport through the bulk of the film towards the hole and electron transport layers.

As discussed earlier, the donor-acceptor nomenclature is quite effective in the context of material combinations with significant HOMO-HOMO and LUMO-LUMO offsets. The best performing OPV devices exhibit small offsets of their HOMO and LUMO levels that result in bidirectional electron and hole transfer (Figure 2.5). The electron-hole pair could form on the donor and subsequently be dissociated via electron transfer to the acceptor. [33,34] Alternatively, if the electron-hole pair are generated on the acceptor, dissociation will occur via hole-transfer to the donor. [34] Hence, the absorption of light by either material results in the generation of holes in the donor and electrons in the acceptor. The electric field in the device leads to the positive and negative charges to move towards their respective electrodes where they are extracted from the device to complete the circuit. As both donor and acceptor produce a photocurrent, it is beneficial to select materials with complementary absorption spectra so as to maximise light harvesting.
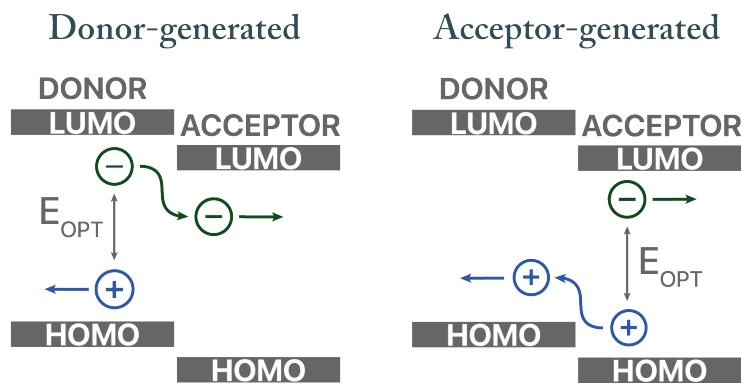

FIGURE 2.5: Photoabsorption (E_{OPT}) results in the transition of an electron from the HOMO to the LUMO and the formation of an exciton.

2.2.4 Minimising charge generation losses

The primary loss mechanism for free charges is the recombination of electrons and holes as a result of discontinuous domains of donor and acceptor. The rate of recombination can be significantly reduced by improving the charge mobility characteristics of the donor and acceptor materials. [35]

Electrons and holes generated in the active layer must be efficiently transported from the donor and acceptor materials to the metallic electrodes via the *electron transport layer* (ETL) and *hole transport layer* (HTL), respectively. Some OPV devices incorporate a transparent HTL such as the polymer blend Poly(3,4-ethylenedioxythiophene)-poly(styrenesulfonate) (PEDOT:PSS) which has good ductility and is easy to process but suffers from stability and reproducibility issues as it is a macromolecular salt. [36] OPV devices can also use a transparent ETL (e.g., zinc oxide) that has high electron mobility and hole blocking properties. [37-39] For devices with transparent ETLs, a metal oxide HTL provides

an energetically desirable pathway for hole collection before the cathode.[40] Ensuring a high quality interface between the active layer and the ETL and HTL is central to good device performance. Using thermal evaporation to deposit metallic layers ensures that the interlayer forms a pore-free interface with the active layer, while the solution-processed charge transport layers typically undergo a thermal annealing post-processing step to produce an optimised morphology.

2.3   Developing next-generation solution-processed devices

For most OPV devices, a donor-acceptor blend ratio of approximately 1:1 to 1:1.5 (by weight) provides the best PCE. When using conjugated polymers and small molecules in BHJ blends at these typical weight ratios, reproducibility and consistency across devices can become difficult due to the inherent variability of the polymer-component molecular weight distribution (known as its dispersity). Minimising the conjugated polymer content in a given active layer while retaining the performance characteristics of the more balanced ratio would be a significant step forward in improving consistency for large area devices. In a commercial setting, where reproducibility at scale is essential for reliable performance, minimising the conjugated polymer component may be an essential step in the path towards producing high performance and long lasting OPV devices.

Low polymer content devices have been shown to exhibit, in the case of polymer:fullerene blends, performance comparable to that of devices fabricated with a more balanced weight ratio.[41,42] Fullerene acceptor materials tend to form an aggregate in the BHJ within which the polymer donor material forms dispersed aggregates. When the polymer content is reduced to approximately 5 wt%, the polymer content is still high enough for an interconnected donor network to form which allows for efficient hole transport.[41] While low donor content devices have been thoroughly studied using fullerene small molecule materials, low donor content NFA systems have yet to be studied in great depth.

The intent of this research project is to study the high-performance NFA materials Y6 and ITIC-2F when blended with a donor polymer at an optimised and low donor weight ratio. Determining how the optical, charge transport and overall device performance properties change when the polymer donor content of the active layer blend is altered will enable an understanding as to why certain acceptor materials can maintain strong performance in low donor configurations. In the broader context, understanding why certain NFA materials are capable of performing well with minimal polymer donor content will provide a basis for further research into these systems with the aim of making efficient large-scale OPV devices with class-leading materials that are highly reproducible. Currently, the fabrication of the best-performing large-scale OPV devices involves the complex blending of multiple organic semiconducting materials to produce an active layer that retains strong performance.[43] Simplifying the active layer blend such that it contains one majority component and minimal quantities of other materials would be an appealing route towards scalable manufacturing of these devices.

The devices fabricated in this research programme utilise organic semiconductor compounds solution-processed as blends to produce thin-films that absorb light. As discussed in the previous chapter, BHJ devices combine organic semiconductors classed as either *donor* or *acceptor* depending on their HOMO or LUMO levels This chapter will provide an introduction to the branch of organic photovoltaic materials of interest for this research programme, NFAs, before discussing the materials selected for this project in greater depth. While the initial focus of OPV research centred on fullerene-based acceptors, current research efforts have been focussed predominantly on the far broader field of NFA materials. [44] Most efficient BHJ devices are mesoscopically phase separated blends of a polymeric donor material and small molecule electron acceptor. [9]

Over the past decade, research into NFA materials have yielded successively higher performance records with the first NFA-based OPV device with a PCE greater than that of the leading fullerene-based OPV devices reported in 2017. [45] It is now possible to exceed 18% efficiency with a BHJ composed of the polymeric donor PM6 and the small molecule acceptor Y6 (two of the materials used in this research study). [46] With this in mind, it is clear that the future of OPV device development lies, in large part, in ensuring that devices can be fabricated more consistently with a view towards better-performing large-area OPVs. Simplifying the composition of the devices by reducing the content of the donor in the active layer blend while retaining strong overall device performance is one such pathway towards these aims.

To successfully commercialise OPV devices, the following criteria need to be met:

Device Efficiency — The PCE of OPV devices must be within a reasonable margin of existing commercially available c-Si PV devices ($\approx$24%). The current efficiency record of 18% PCE indicates that this criteria should be achievable in the near future and modelling of BHJ systems indicates a maximum achievable PCE of 23%. [47]

Manufacturing Scalability — For the greatest scalability and lowest production cost, an ideal OPV device will be solution processable.

Device Lifetime — Commercially available OPV devices must be able to withstand the solar radiation and thermal stress as a result of regular exposure to the sun. Once the efficiency target has been reached, it will be necessary to continue the development of further-refined junction materials so as to minimise degradative losses.

As discussed in the next section, the ability to molecularly engineer NFA materials lends itself well to further innovation in this space that will push device efficiency and lifetime forwards to the point where commercial-scale manufacturing of OPV devices is economically viable. Analysing the effect on device performance when changing parameters such as the donor polymer concentration in the active layer blend can reveal useful information on the ways in which lab-fabricated device performance can be replicated on larger scales.

3.1 Non-fullerene acceptor design principles

The recent focus of acceptor material design, synthesis and testing has focussed on innovation into new classes of NFAs that address some of the longstanding limitations of fullerene acceptor materials.[10] NFAs bring with them a swathe of unique paradigms that set them apart from the first generation of fullerene-based OPV acceptor materials:[9]

Greater Control Over Molecular Design — Morphologically, most NFAs are predominantly planar, however the core and functional groups that can be used are far more diverse than for fullerene materials which open up a broader array of molecular design strategies to produce desirable material characteristics.

Advantageous Morphology — The planarity of NFAs such as Y6 can lead to more predictable and controllable packing characteristics. This leads to improved light absorption, charge transport and long-term stability.[48]

Improved Charge Generation — Exciton dissociation can occur with high efficiency in blends incorporating NFA materials as the energetic offsets between materials in the junction can be tuned to be less than 10^{-1} eV. Recent literature has suggested that the paradigm of CT states used to describe the transfer of energy between different materials used in BHJ films may not apply to some of the highest performing NFAs.[49,50]

Improved Absorption Characteristics — The absorption characteristics of NFA materials can be tuned through the addition of functional groups and electronegative atoms so as to more effectively complement the absorption spectra of the donor material.

Stability and Thick Junction Performance — The latest generation of high-performance NFAs have shown to also have better performance in thick BHJ devices ($\geq$ 300 nm) as a result of a combination of the other characteristics listed above, particularly when considering BHJ morphology.

3.2 NFAs used for this study

3.2.1 ITIC-2F

A successful molecular design strategy has involved integrating functional groups that act as acceptor (A) and donor (D) units where combination determines the absorption spectra, ionisation potential and electron affinity.[51] First, introduced in 2015, 3,9-bis(2-methylene-(3-(1,1-dicyanomethylene)-indanone))-5,5,11,11-tetrakis(4-hexylphenyl)-dithieno[2,3-d:2′,3′-d′]-s-indaceno[1,2-b:5,6-b′]dithiophene (ITIC) was one of the first NFA materials that could surpass the performance of fullerene acceptors when used to fabricate OPV devices.[52] The ITIC-family of NFA materials have become a popular testbed for many iterations of side-chain and end-group modifications which have led to further fine

tuning of molecular energy levels and packing behaviour.[15,34,53,54]. Alternative structural arrangements, including D-A-D, D-A-A-D and D-A-A have also been trialled through modification of the ITIC backbone.[55,56] Introducing additional fluorine atoms, the most electronegative atom with the smallest atomic radius, to the basic ITIC structure has been another very successful molecular design strategy.[45,57,58] Fluorination of acceptor molecules have been associated with a range of overall performance enhancements.

- Stabilising the HOMO-LUMO levels without strong steric hindrance (significant structural deformations due to the addition of bulky end-groups).[59]

- Non-covalent interactions between fluorine and other atoms both intra- and inter-molecularly have been correlated with improved crystallinity and, by association, higher rates of charge transport.[60]

- Fluorinated molecules also tend to have a reduced Coulombic potential which dampens the rate of of exciton recombination.[60]

- Some fluorinated molecules exhibit better light absorption characteristics than their non-fluorinated equivalents.[61]
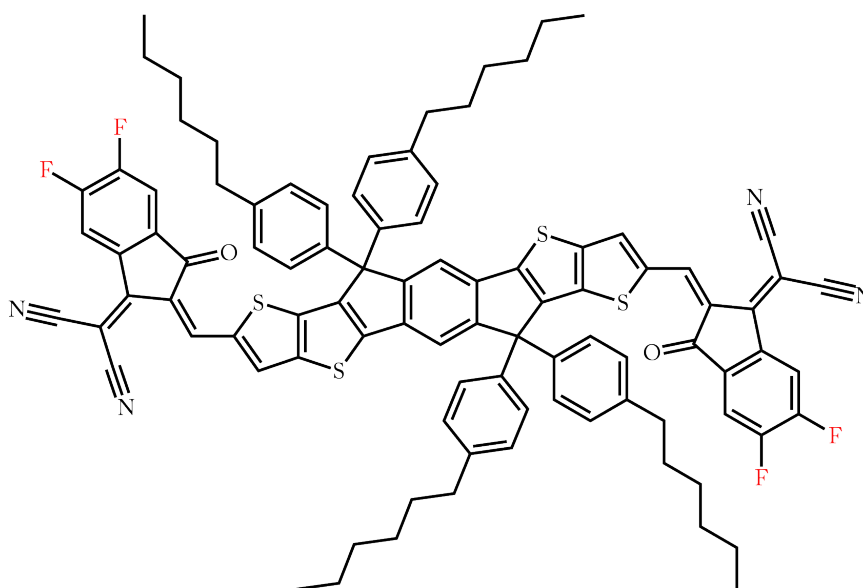
FIGURE 3.1: The ITIC-2F chemical structure with additional fluorine atoms highlighted in red.[62]

3.2.2 Y6

First introduced in 2019, 2,20((2Z,20Z)((12,13-bis(2-ethylhexyl)3,9-diundecyl-12,13-dihydro[1,2,5]-thiadiazolo[3,4e]thieno[2,"30 ′:4′,50] thieno[20,30:4,5]pyrrolo[3,2g]thieno[20,30:4,5]thieno[3,2b]-indole-2,10-diyl)bis(methanylylidene))bis(5,6 -difluoro-3-oxo-2,3-dihydro-1H-indene-2,1-diylidene)-)dimalononitrile (Y6) is currently the best performing commercially available small molecule acceptor material, with a maximum recorded PCE of 17.1%.[14,63] Despite the small driving force of exciton generation in BHJ blends utilising Y6, efficient charge generation is still achieved as the large electrostatic interfacial field enables high efficiency CT state dissociation.[49] The high degree of crystallinity that Y6

exhibited in a BHJ configuration has also been attributed to its high performance, with the formation of (relatively) ordered polycrystalline structures that have been analogised with unit cells of inorganic semiconducting materials. [63,64]. Further work has produced functional derivates of Y6 with additional alkyl or alkoxy groups that can be used in conjunction (in so-called *ternary* devices) with the original compound to produce an enhanced energetic cascade that facilitates efficient charge transport. [65] The discovery of the ability for Y6 to form polycrystalline domains has spurred a series studies looking to push this in the pursuit of improved PCE, stability and thick BHJ performance. [64,66–69] Y6 has also been blended repeatedly with fullerenes (as the latter's tendency to favourably aggregate under thermal annealing has been thoroughly studied) to produce so-called *hierarchical* morphologies that can be further enhanced using thermal annealing as a post-processing step to produce *quaternary* devices with efficiencies of approximately 17.6%. [70] The rapid development of high-performance Y6-family acceptor materials has also spurred on research into new wide-bandgap polymer donors that utilise some of the structural motifs that have made this material family so successful thus far. [71]
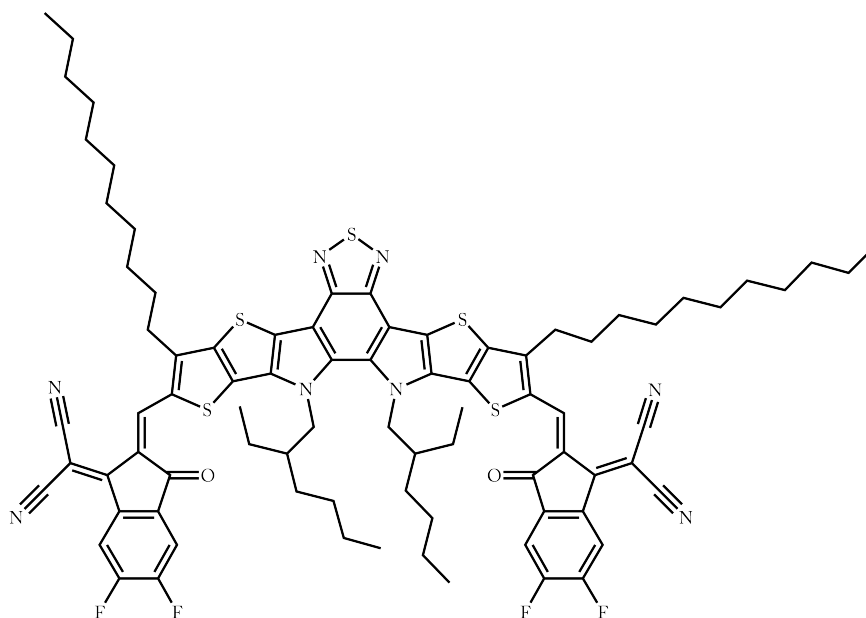
FIGURE 3.2: The Y6 chemical structure. [72]

Table 3.1: Y6 General Data[72]

CHEMICAL FORMULA	$C_{82}H_{86}F_4N_8O_2S_5$
MOLECULAR WEIGHT	1451.93 g·mol^{-1}
HOMO	-5.65 eV
LUMO	-4.10 eV

This research programme involved the fabrication of OPV devices to assess the impact of altering the donor polymer weight concentration in the active layer. OPV devices were fabricated in a range of configurations using the selected donor and acceptor materials to quantify how changes to the active layer blend ratio and deposited layer thickness affected overall performance. To complement the iterative process of device fabrication, a suite of thin-film analysis techniques were utilised to quantify their parameters. Using the suite of thin film characterisation and device performance data, an understanding of how the polymer content of an OPV solution affects overall photovoltaic efficiency can be obtained.

4.1 Materials Preparation

All materials used as part of this research programme were acquired commercially. The donor polymer, PM6, was purchased from 1-Material Inc. and the NFA materials, Y6 and ITIC-2F, were purchased from Ossila. The diethyl zinc precursor solution and all solvents used were supplied by Sigma Aldrich. ITO-patterned device substrates were obtained from Xin Yan Technology Limited.

4.2 Device Fabrication and Performance Optimisation

4.2.1 Fabricating an organic photovoltaic device

OPV devices were fabricated to test the performance of active layer materials under various processing conditions. The standard steps of the fabrication procedure for an OPV device are described here and the specific procedures for each device type studied in this research programme have been included in Section 5.1.1. Fabrication of all high-performance organic semiconducting devices occurred in a Class 1000 cleanroom environment[a]. As many of the materials used in OPV devices are moisture- and oxygen-sensitive, most stages of the fabrication process were carried out in nitrogen-filled gloveboxes that scrub the internal atmosphere of oxygen, water and other solvents that are used during the fabrication process.

---

[a]Most dust particles being on the order of $\times 10^2$ greater in size than the thin-films produced in this process. The cleanroom facility at COPE has been designed to meet the Class 1000 standard which means that there are less than 1000 particles of dust per cubic metre inside the laboratory.

4.2.1.1 Preparing the substrate for spin-coating

The substrates used for OPV device fabrication were acquired commercially for large batch consistency with the *indium tin oxide* (ITO) layer pre-patterned on the 15mm^2 glass substrates. To protect the ITO layer from scratches and residues, a polymer layer is applied during manufacturing (Figure 4.1). Once this polymer film had been removed, the substrate was not yet ready to use as the ITO-facing surface still had a significant amount of polymer residue on the surface that needed to be removed along with any fine particulate matter that has been trapped on the surface during the manufacturing process. Debris remaining on the surface of the substrate causes inconsistencies in the spin-coated thin-films and device shorting.

To prepare the substrates, a common sequential wet and dry cleaning process was used:

1. Using Alconox, a strong biodegradable detergent, most of the contaminants from the substrate were removed. An eighth of a teaspoon of Alconox crystals were added to approximately 100 mL of *deionised* (DI) water in a broad-base beaker which was then brought to 70 °C on a hot plate. Once the substrates were placed (ITO-side up) in this solution, they were left for ten minutes.

2. The substrates were then sequentially sonicated in Alconox, DI water, acetone and IPA for 10 minutes, respectively. Sonication uses compression waves at ultrasonic frequencies in a fluid bath to agitate and remove debris from the substrates.[73]

3. The substrates were removed individually from the IPA beaker and dried with pressurised nitrogen, taking care to aim the stream away from the tweezers used to hold the substrate so as to avoid contaminating the substrates, which are now particulate-free. At this stage of the process, the substrates were inspected and disposed of if large scratches or smears from the polymer coating remained.

4. The substrates were then placed in an ultraviolet-ozone (UV-O$_3$) cleaning system where they were left to complete a 30 minute cycle. This process is designed to remove any remaining organic contaminants on the substrate prior to deposition of the next layer. A low-pressure mercury discharge tube generates two dominant emission peaks in the ultraviolet region. The shorter-wavelength spectral line (184.9 nm) decomposes oxygen molecules, resulting in the formation of two radicals of oxygen that subsequently react to produce ozone (O$_3$). The longer-wavelength spectral line (253.7 nm) excites organic contaminants present on the substrate surface, which increases their reactivity with ozone, which results in the formation of volatile species (e.g., carbon dioxide or water) that desorb from the surface of the substrate.[74] This dry cleaning method is only effective if the substrates have already been processed through wet cleaning as it works most efficiently on monolayers of organic compounds remaining after the bulk of the contaminant matter has already been removed.

4.2.1.2 Charge Transport Layer Solution Preparation

Once the substrates were cleaned, the next step was to prepare the solutions for subsequent layer deposition by spin-coating. The first spin-coated layer was either a solution-processed ETL or HTL (Figure 4.2). For conventional structure devices, PEDOT:PSS was used for the HTL and was prepared by a process of filtration to eliminate aggregates larger than 0.45 μm. A solution processed ETL, 2,9-Bis[3-(dimethyloxidoamino)
propyl]anthra[2,1,9-def:6,5,10-d′e′f′]diisoquinoline-1,3,8,10(2H,9H)-tetrone (PDINO), was prepared by dissolving the compound in methanol at a concentration of 1.5 mg/mL.

(a)

(b)

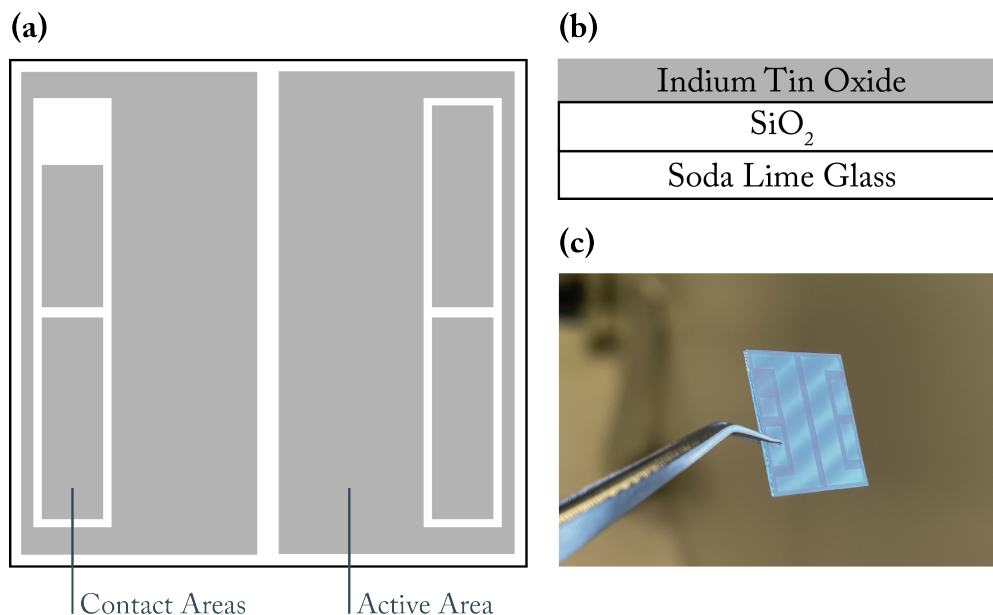| Indium Tin Oxide |
| SiO$_2$ |
| Soda Lime Glass |

(c)

Contact Areas   Active Area

FIGURE 4.1: (a) The patterned ITO on glass substrate used to fabricate the OPV devices (ITO areas shown in grey). The patterned sections on the left and right sides of the substrate connect with the electrical contacts of the device testing system. (b) The layer structure of the ITO substrates with the 100 nm thick patterned ITO sputtered-coated on top of the naturally occurring silicon dioxide layer of the soda lime glass. (c) A substrate used to fabricate OPV devices with the sputtered ITO layer viewed from an oblique angle.

In the case of the ETL for an inverted structure device, zinc oxide was used due to its optoelectronic properties and the fact that it does not dissolve during subsequent layer deposition. To prepare the zinc oxide solution for deposition, 1.0 M diethyl zinc (suspended in hexane) was diluted with tetrahydrofuran (THF) in a 1:7 volume ratio. This produces a dilute precursor solution that can be spin-coated directly onto the cleaned ITO substrates.

4.2.1.3 Active Layer Solution Preparation

The active layer blends were prepared as follows:

1. Active layer solutions are prepared in a 1.5 mL vile in a nitrogen-filled glovebox. Approximately 3-10 mg of the donor polymer and acceptor molecule are weighed out using a microbalance and chloroform was then added.

2. The solutions were left to blend for at least two hours with moderate heating ($\sim 70°$C) to ensure both components were thoroughly dissolved in the selected solvent. If the selected materials or blend ratio had not been trialled before, it was helpful to check for large particles remaining suspended in the solution at regular intervals and adjust the temperature, stirrer bar spin-speed or dilution as required.

(a) Conventional
STRUCTURE

(b) Inverted
STRUCTURE

hν

hν

Cathode	*Ag*	~100nm
ETL	PDINO	~10nm
Active Layer	PM6:Y6	~100nm
HTL	PEDOT:PSS	~10nm
Anode	ITO	~100nm

Anode	*Ag*	~100nm
HTL	*MoOx*	~10nm
Active Layer	PM6:ITIC-2F	~100nm
ETL	ZnO	~10nm
Cathode	ITO	~100nm
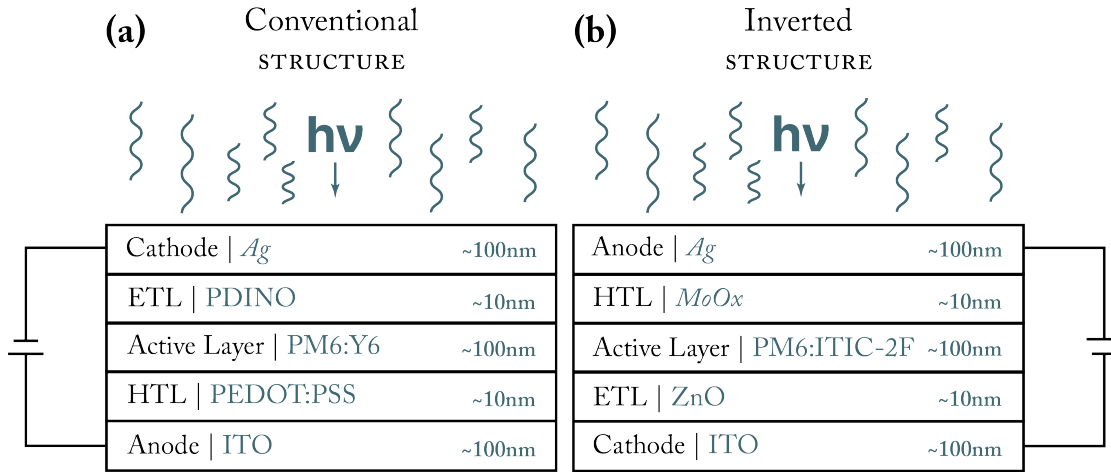
FIGURE 4.2: The device structures where the ITO serves as (a) the anode and (b) the cathode. Noted in green for both diagrams are the materials used for each layer with solution-processed layers typeset in roman and thermally evaporated layers italicised.

4.2.1.4 Thin-film fabrication using spin-coating

The next step, spin-coating, is the simplest method to coat small area (typically <25 cm^2) substrates by spinning the substrate (typically at 1000-5000 rpm for 30-60 seconds) such that the deposited solution spreads evenly across the surface before drying. Spin-coating solutions onto the substrate requires careful control of the spin speed and time to ensure that the desired thickness is achieved along with a high film quality. A good spin-coated thin-film should be glassy in appearance, have no debris causing "comet tails" on the surface of the film, and should be visibly dry at the conclusion of the process (Figure 4.3).[75,76] When trialling a new material combination or blend ratio, it is usually necessary to perform a series of tests at this stage to ensure the desired film characteristics are achieved (Table 4.1). For a new active layer blend, optimising the layer thickness to achieve the optimised device performance (with most active layers being ~80-120 nm thick) requires a process of iteration with an understanding of the rate at which the solvent evaporates from the substrate and the approximate molecular weights of the compounds in the blend. If it was the first time that a particular active layer solution has been trialled, the thickness of the spin-coated layer on glass was typically checked using a surface profilometer before proceeding with the cleaned substrates. The following process was used for solution-processing device layers.

1. A clean substrate was placed on the vacuum chuck, which holds the substrate in place during the spin-coating process.

2. Using a variable volume pipette, a small volume of the solution ($\sim$30-120 μL for 15 mm^2 substrates) was then deposited on the substrate in a carefully controlled stream beginning from the centre, which ideally forms a meniscus around the perimeter prior to starting the predetermined spin programme. Bubbles left on the surface of the substrate from an incomplete draw of the stock solution with the micropipette, uneven coatings due to improperly dissolved or overly viscous solutions and incomplete coverage of the substrate as a result of the rapid evaporation of a highly-volatile organic solvent can affect the final film.

3. Immediately after the solution had been deposited on the substrate, the spin-coater was started and accelerates to the set rotation rate before remaining there for the set time and rapidly de-

celerating at the end of the cycle. During the initial phase of angular acceleration, most of the solution ($\sim 90\%$) is expelled from the substrate. The residual solution will become level when the fluid is rotating with the same angular velocity as the substrate.

4. The spin-coated substrate was then removed from the chuck and left to dry while the process was repeated for the remaining substrates. Once all the substrates had been spin-coated, the edges with patterned ITO contacts were then wiped with the same solvent used for the spin-coated solution to ensure the ITO could make contact with the testing apparatus.

5. The substrates were then transferred to a hot plate to be thermally annealed. This process introduces additional thermal energy to the thin-film which may assist molecular rearrangement and the formation of structural features such as polycrystalline domains. [70]

For the zinc oxide ETL layer in inverted devices, it was necessary to first optimise the layer thickness. [37] The diethyl zinc used for this experimental investigation was dissolved in hexane at a 1.0 M concentration whereas previous zinc oxide solutions were prepared using 1.5 M solutions with toluene as the solvent. To determine the effect of using a different solvent and diethylzinc concentration, an ITO substrate was spin-coated with a 1:7 volume dilution of the new diethylzinc in hexane diluted with tetrahydrofuran at 5000 rpm for 30 seconds in the glovebox before being annealed at 150 °C for 15 minutes in air. *X-ray reflectivity* (XRR) was then performed on both a clean ITO substrate and the ZnO-coated ITO on glass substrate to measure the layer thickness which was determined to be 4 nm. To reach the desired layer thickness of approximately 10nm, the same 1:7 dilution was retained and the spin-speed reduced to 1500 rpm for 30 seconds before thermal annealing. Complete devices were then fabricated using this new ETL and benchmarked against published device performance data for PM6:ITIC-2F OPV devices.

Table 4.1: Common issues encountered whilst spin-coating the solution-processed layers.

Issue	Possible Cause	Resolution
Improper Surface Coverage	The solution may be too viscous, the solvent quite volatile or not enough blend solution has been deposited on the surface.	Dilute the solution and/or increase the spin-speed.
Uneven Surface Height	The solution may be too viscous or the solvent has begun to dry in some regions before the entire substrate is wetted.	Deposit the solution rapidly from the centre outwards to avoid premature solvent evaporation.
Agglomerations & Rough Films	Large particles may remain after solution preparation if the selected materials have not fully dissolved in the selected solvent.	Heat the solution during the preparation stage and/or filter the blend solution prior to spin-coating.

4.2.1.5 Evaporation of Electrodes

The final stage of the OPV device fabrication process was to thermally evaporate metallic electrodes onto the surface of the active layer using a high vacuum thermal evaporation system (Figure 4.4). In an inverted structure device, this meant using a thermally deposited molybdenum oxide to create a HTL before depositing a silver cathode layer to complete the energetic cascade discussed in Section 2.2.1. For a conventional structure device, silver was used as the metallic capping layer.
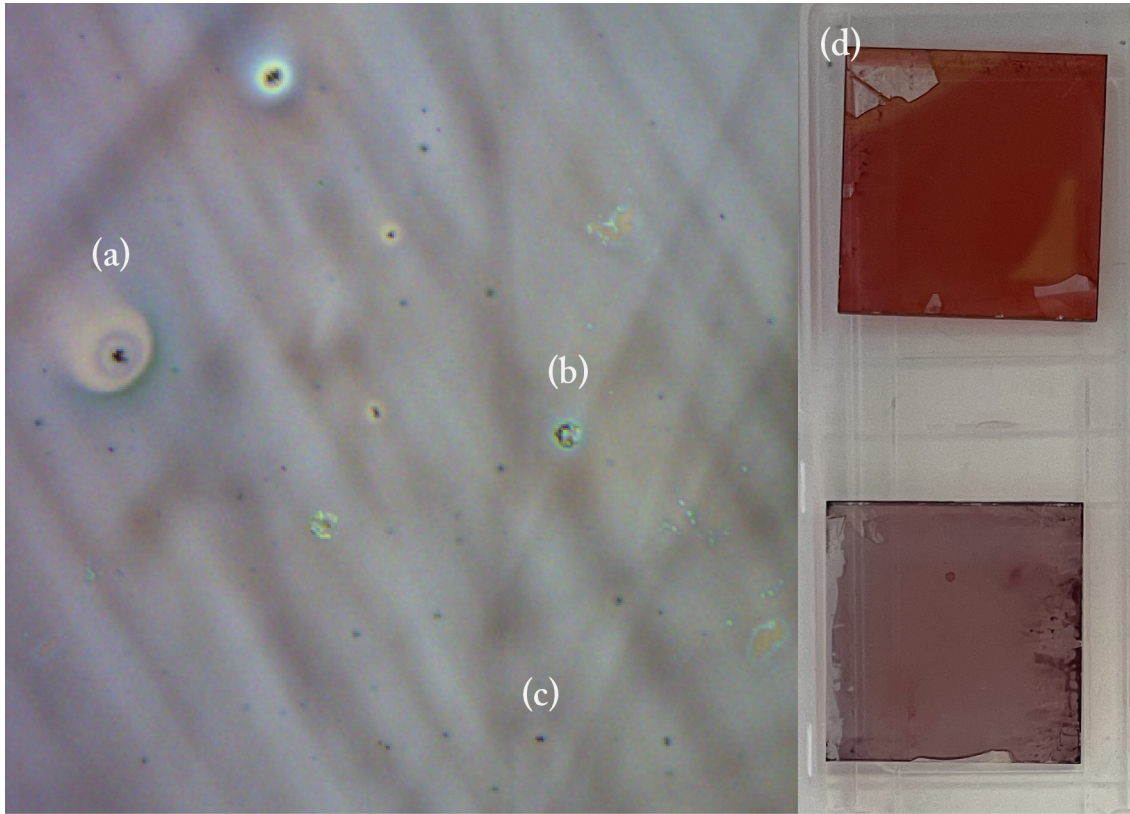
Figure 4.3: An optical microscope image of a thin-film fabricated for an OPV device. (a) A *comet-trail* caused by dirt already on the surface of the film that obstructed the complete coating of the surface. (b) A surface contaminant on the order of a few microns high that can result from film exposure outside the cleanroom. (c) Prior to spincoating the PEDOT:PSS hole transport layer, the dispersion is passed through a 0.45 μm filter that removes all particles greater than this size, with some agglomerations remaining and visible here as small black dots across the surface. (d) Two low-quality films produced using a perylene diimide material. High solution viscosity meant that the solution did not spread evenly to the edges of the substrate during spin-coating.

The thermal evaporator is a chamber that, once the substrates are loaded onto the sample holder, is brought to a very low pressure ($\sim 10^{-6}$ bar over the period of an hour) (Figure 4.4). At this low pressure, the mean free path of evaporated atoms and molecules is over a meter, allowing for their free passage through the chamber (a vacuum is also critical for high film purity). The metal oxide and metal were vaporised by Joule heating in a resistive container (the former in a ceramic crucible and the latter in a tungsten boat) where atoms and molecules then nucleate on the top surface of the thin films at $\sim 0.5 - 1.0$ Å·s^{-1}.[77] The HTL was deposited with a thickness of 10 nm, while the metal cathode was deposited with a final thickness of 100 nm. During each evaporation cycle process, the rate of deposition must be carefully controlled to avoid evaporating too quickly which will result in voids in the electrodes. Excessive heating in the evaporator (> 70 °C) as a result of excessive evaporation rates can also damage the temperature-sensitive organic thin-films. Once thermal evaporation was complete, the devices were ready to be transferred to the testing glovebox (Figure 4.5).
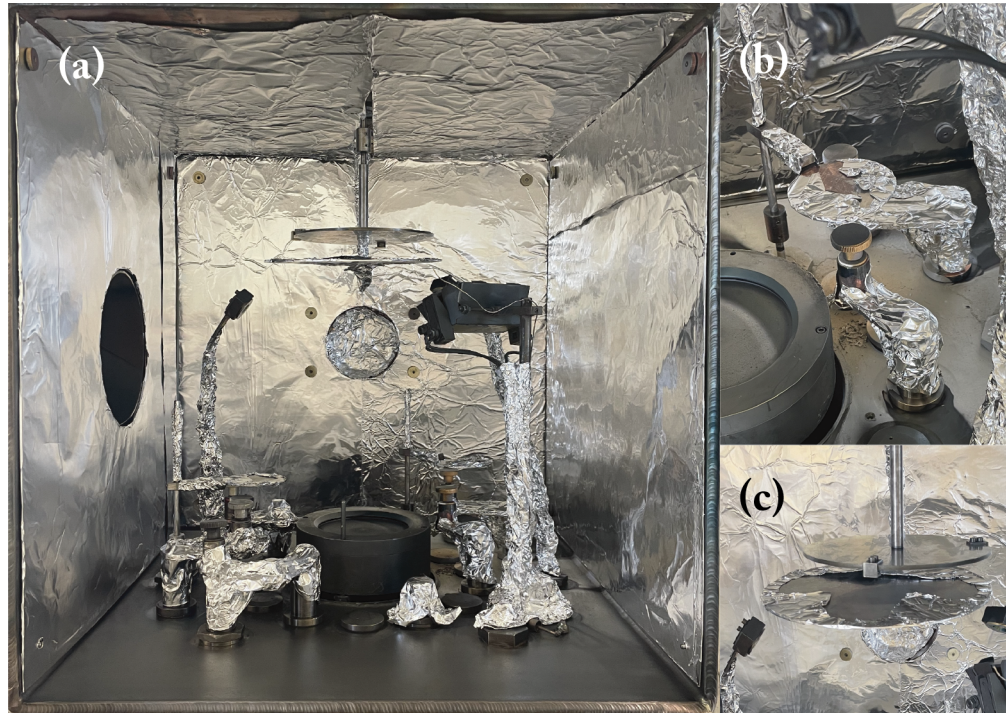
FIGURE 4.4: (a) Inside the evaporation chamber where the crucible and boat holders (lower left and right, respectively), rotating mount (top centre) and vacuum pump port (left wall) are visible. (b) The mounts for the crucible where the tungsten boat is installed and metal pellets are added that are then melted during the evaporation cycle to produce the metallic vapour that strikes the substrate surface. (c) The rotating mount that the substrate mask is attached to that ensures an even distribution of metal atoms across each substrate.
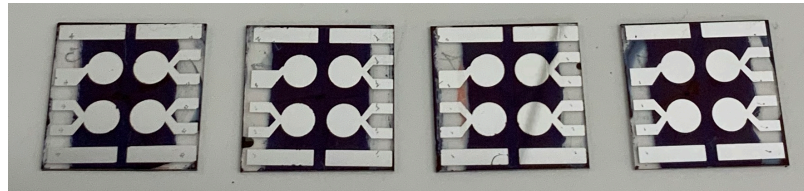
FIGURE 4.5: A selection of completed devices fabricated using the above procedure. Each device has been fabricated on an ITO-sputtered glass substrate, in this case with a transparent PEDOT:PSS hole transport layer, deep purple active layer and silver electrodes patterned on the surface via thermal evaporation.

4.2.2 Measuring the performance of complete devices

4.2.2.1 The solar spectrum

Before describing the process for testing the photovoltaic performance of complete devices, it is informative to first provide context on the solar spectrum that supplies the photon flux required for the energy conversion process to occur. The spectrum of a light source contains the information needed to determine the relative population of photons at given wavelengths. From this information, it is possible to determine the energy flux density of the light source. In the case of the solar spectrum, the spectral irradiance emitted by the Sun that is incident on Earth's atmosphere is measured. Before in-

cident light from the Sun passes through the atmosphere, the spectrum is denoted *air mass* (AM) 0.[78] The modified solar spectrum that takes into account the distance the incident photons travel through the atmosphere corresponding to an angle of incidence of 48° is denoted as AM 1.5 and is the standard spectrum used for characterising all photovoltaic devices. The total energy flux density at AM 1.5 is defined as 1 kW/m^2, which is a good approximation for the average value measured on the Earth's surface[b].[78] As will be discussed in greater depth in the next sections, ensuring optimised absorption in the wavelength range with greatest spectral irradiance is an important design strategy for all OPV materials. In the case of the low donor content devices fabricated as part of this research project, the aim was to retain good absorption across the solar spectrum whilst minimising the polymer content in the active layer. Once the devices were completed, they were ready to be tested using the solar sim-
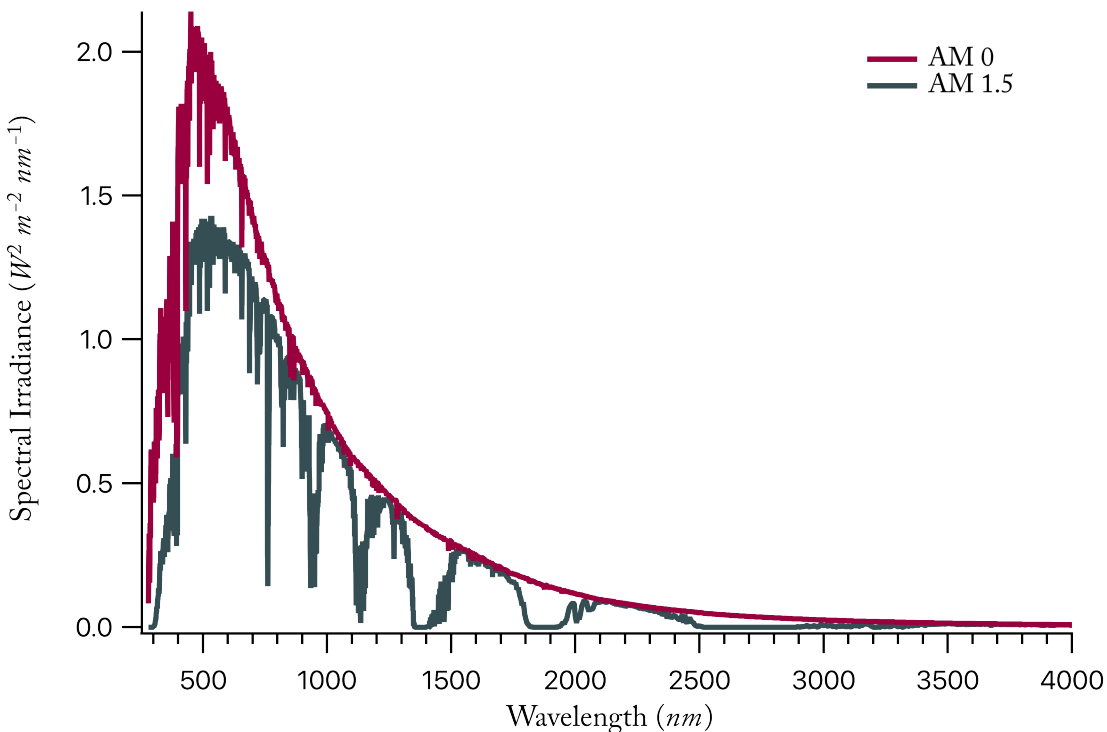
FIGURE 4.6: Spectral irradiance for the solar spectrum as a function of wavelength (λ). This example presents both AM 0 and AM 1.5, the spectral irradiance prior to passing through the atmosphere and the standard spectrum used to test terrestrial PV devices, respectively.[78]

ulator that provided an AM1.5G spectrum with appropriate flux. A xenon arc lamp coupled with an air mass filter precisely matches the spectral output of the lamp with the solar irradiation spectrum (as discussed in Section 4.2.2.1).[79] The OPV device was held in a mount with integrated electrical contacts that complete the circuit from the cathode and anode to the test station, which was then used to determine the photocurrent produced by the 0.08 cm^2 active area of the connected device (Figure 4.7). A voltage control system sweeps from -1 V to 1 V and the current generated by the connected device was measured at each step with an ammeter connected in series (Figure 4.8).[80]

These metrics were then used to calculate key parameters for the device that allow for direct comparison with devices made previously.[17] The parameters include:

---

[b]If we were to model the total energy flux density exclusively at the poles or in equatorial regions, the intensity would of course be greater. The AM 1.5 model provides a useful average for locales situated in the mid-latitudes.

Short Circuit Current Density (J_{SC}) — The current through the device when the bias across anode and cathode is zero. At this point, the flow of current is dependent on the photon flux incident on the active layer. As short circuit current is dependent on the area of the device, removing the area dependence produces a metric that can be more readily compared. A change in J_{SC} can indicate an altered absorption efficiency (e.g., due to spectral overlap or layer thickness) or exciton diffusion rate due to changes in the bulk morphology of the active layer or interfaces.[32] In this sense, J_{SC} is representative of the overall conversion efficiency of photons to charges.

Open Circuit Voltage (V_{OC}) — At the open circuit voltage, measured voltage is at a maximum and current is zero. V_{OC} corresponds to the forward bias on the device as a result of current generated from incident solar radiation. V_{OC} is correlated with the interfacial morphology between donor and acceptor and the energy offset between these materials. A change in V_{OC} may be the result of a changed charge generation rate or charge collection efficiency at the electrodes.[50]

Fill Factor (FF) — The fill factor gives the ratio of maximum outputted power and $J_{SC}V_{OC}$ (see Equation 4.1). FF is dependent on the charge generation properties of the active layer such as the overall charge mobility, rate of charge recombination, probability of exciton dissociation and overall incident light absorption. A high FF indicates that carrier mobility is high and rates of recombination are low with an ideal device exhibiting a *fill factor* (FF) of one.[17] FF can be calculated with the relation,

$$FF = \frac{P_{max}}{J_{sc}V_{oc}}. \tag{4.1}$$

Power Conversion Efficiency (PCE) — The ratio of maximum generated power and incident power (I_{in}). This metric is most quoted in the literature as it provides a direct point of comparison between other OPV devices and energy generation techniques that utilise other technologies. The diagnostic usefulness of PCE is limited, however, as it can obscure underlying physical phenomena that can affect device performance. PCE can be described by,

$$PCE = \frac{J_{sc}V_{oc}FF}{I_{in}}. \tag{4.2}$$

Once the light response of the OPV device has been determined, closing the shutter on the lamp to perform a dark current and voltage measurement with injected (rather than light generated) carriers can provide further diagnostic information about the device.[81] If it is assumed that the *external quantum efficiency* (EQE) of the device is independent of voltage, then the dark current at V_{OC} should be equivalent to the photocurrent under illumination.[17]

Shunt Resistance (R_{SH}) — A measure of the propensity for current loss in the device. A low shunt resistance indicates that alternate current paths exist for the light-generated current. The formation of local shunts at interfaces due to high crystallinity (and therefore increased surface roughness) or noncontinuous layers can severely impact the overall performance of the device.[82]

Series Resistance (R_{SE}) — Quantifies the resistance provided by each layer of the device. R_{SE} is a limiting factor of V_{OC} and FF.
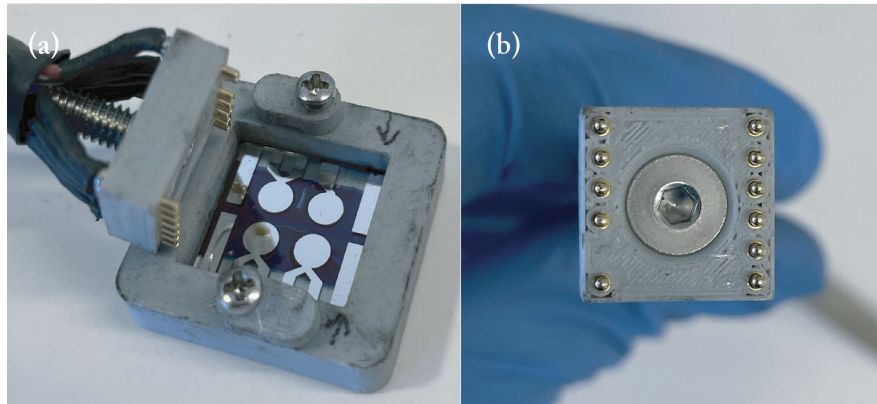
Figure 4.7: (a) An OPV device mounted in the substrate holder ready for testing with the pins of the testing mount visible that are arranged to align with the device electrode pattern. (b) A face-on perspective of the testing system electrodes.
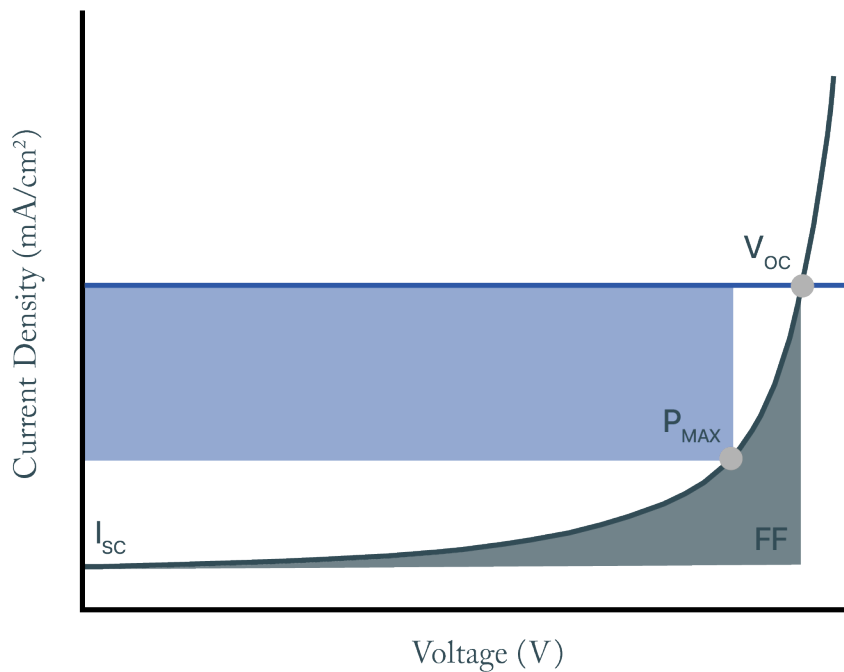
Figure 4.8: Current density-Voltage (J-V) measurements are the first step in OPV device characterisation and enable the fast identification of the best cells (and cell-pixels) for further analysis. Short circuit current density (J_{SC}), open-circuit voltage (V_{OC}), fill factor (FF) and power conversion efficiency (PCE) are derived from the J-V curve.

4.2.3 Measuring the external quantum efficiency

A coherent variable-wavelength light source can be used to directly measure the EQE of an OPV device. The EQE system is designed to measure the population of charge carriers collected from the device in response to a known rate of monochromatic light that is incident on the active layer. The EQE response should resemble the UV-Vis spectra of the film and integrating under this curve will give the I_{sc}, which can be used to calculate the J_{sc} for direct comparison with solar simulator measurements.

This measure of overall efficiency is described by,

$$\text{EQE}(\lambda, V, T) = \eta_{\text{PA}}(\lambda) \cdot \text{IQE}(\lambda, V, T), \tag{4.3}$$

where η_{PA} is the photon absorption efficiency. The *internal quantum efficiency* (IQE) is the ratio of charge carriers produced by the OPV device in response to a given number of absorbed photons.[17] This relationship can be written as a product of efficiencies,

$$\text{IQE}(\lambda, V, T) = \eta_{\text{PA}} \eta_{\text{ED}} \eta_{\text{CT}} \eta_{\text{CD}} \eta_{\text{CP}} \eta_{\text{CC}}.\text{[17]} \tag{4.4}$$

$\eta_{\text{PA}} \rightarrow$ Photon absorption efficiency

$\eta_{\text{ED}} \rightarrow$ Exciton diffusion efficiency

$\eta_{\text{CT}} \rightarrow$ Charge transfer state formation efficiency at the photoactive compound interfaces

$\eta_{\text{CD}} \rightarrow$ Exciton dissociation efficiency in the donor and acceptor

$\eta_{\text{CP}} \rightarrow$ Charge transport efficiency through the active layer bulk

$\eta_{\text{CC}} \rightarrow$ Charge collection efficiency at the electrodes
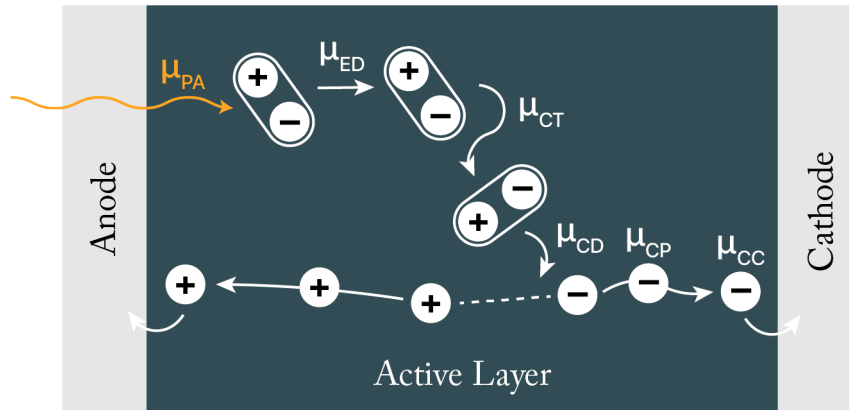
FIGURE 4.9: IQE is the product of efficiencies that describe each stage of the charge generation process.

4.3 Materials Analysis

When studying a new material or blend for OPV applications, it is first necessary to determine the optical properties of thin-films similar to those fabricated for complete OPV devices. This enables the identification of the following optical properties:

Absorption Spectra — Measuring the absorption spectra of both neat films (i.e., just one component of the active layer) and heterojunctions with polymeric donor and small molecule acceptor in varying ratios will indicate which blends absorb most strongly and how the introduction of the donor may influence the absorption spectra.

Optical Constants — Determining the refractive index and extinction coefficients of a thin film means that it is possible to perform computational optical modelling that will predict the optimal thickness of a device to maximise current density and the charge generation rate within the bulk heterojunction. Also of interest is the calculation of the dielectric constant that provides an insight into the Coulombic interactions between photo-generated charge carriers.[83]

The film morphology and the analysis of the ways in which neat and blend films undergo a process of molecular packing and arrangement during the spin-coating process is also important for understanding the device performance. The following structural characterisation methods were used:

X-Ray Reflectometry (XRR) — Reflected X-ray signals can be used to determine the thickness, density and roughness of films, such as the ones fabricated in this research programme. The intensity of light scattered by a thin-film is proportional to the square of the absolute value of the of the Fourier transform of the electron density. Using the data fit parameters, the scattering length density can be calculated, which is a proxy for the actual film density.

Grazing-Incidence Wide-Angle X-ray Scattering (GISAXS) — A structural measurement technique that can probe on molecular length scales to determine the orientations of constituent materials and their distribution as a result of changes to the material content.

Atomic Force Microscopy (AFM) — Using a probe with a radius of approximately 15 nm, *atomic force microscopy* (AFM) can be used to measure the surface topology of a thin-film, which provides information on the effect of different material concentrations on the average surface roughness for micron-scale area surveys.

4.3.1 Determining the optical constants

4.3.1.1 Fundamentals of ellipsometry

The optical constants were measured using *variable angle spectroscopic ellipsometry* (VASE) (Figure 4.10). This technique can also be used to determine other characteristics of thin films spin-coated on silicon, including the crystallinity, optical anisotropy and thickness.[84] Ellipsometry has a greater accuracy than intensity reflectance measurements as absolute intensity of the reflected beam is not a parameter of interest. The measured values, denoted Ψ and Δ are related to the Fresnel reflection coefficients R_p and R_s which are given for parallel and perpendicularly polarised light by,

$$\rho = \frac{R_p}{R_s} = \tan(\Psi)e^{i\Delta}, \tag{4.5}$$

where the phase (Δ) is a complex number which introduces a phase component to the measurement. Ellipsometry measures the ratio of these values, which significantly reduces the propagated error.[84] The ellipsometry technique used to determine the optical constants for the organic materials of interest is known as VASE. The core advantage of this approach when compared with intensity reflectance is that the latter is confined to a normal incidence which provides a single datapoint at each wavelength step whereas VASE can operate over a range of angle steps from the normal. Along with the aforementioned enhanced sensitivity of ellipsometry, the increased number of parameters that can be determined means that this approach can be used to determine a greater range of material parameters.

4.3.1.2 Ellipsometry Sample Preparation & Measurement

Samples for the ellipsometry measurements were prepared on silicon substrates. Solutions of neat PM6, Y6 and ITIC-2F were prepared in chloroform with total concentrations of 9 mg/mL. Blend solutions of PM6:ITIC-2F and PM6:Y6 were prepared in chloroform with total concentrations of 10-12 mg/mL. The blend solutions were prepared with a lower concentration than for the active layer films so as to reduce the final film thickness. All samples were spin-coated at 5000 rpm for 30 seconds before the blend films were subsequently annealed at 110 °C for 10 minutes in the glovebox. Neat films were left as-cast.
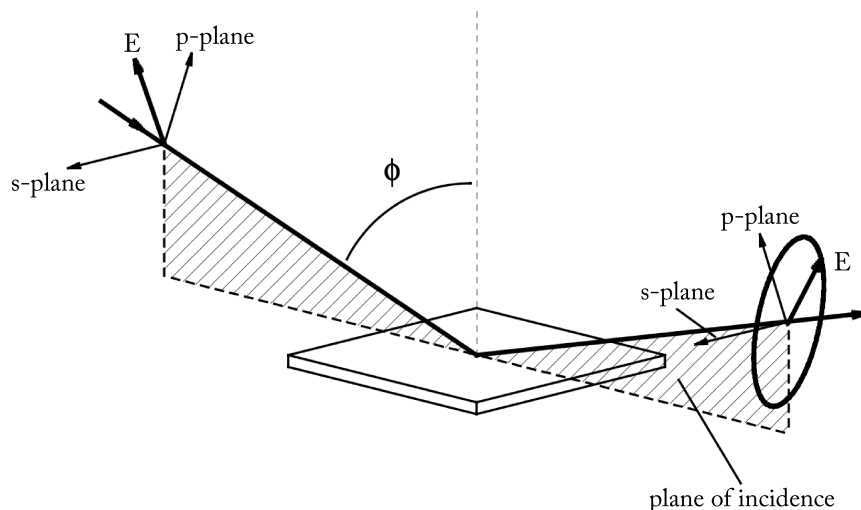
FIGURE 4.10: Geometry of an ellipsometry measurement with the associated s and p light polarisation states (adapted from J. A. Woollam Co., Inc.).

Producing sub-100 nm thick films that are uniform across the surface is critical for reliable ellipsometry measurements. As organic semiconducting materials are highly absorbing across the visible spectrum, minimising the film thickness ensures that the polarisation state of light reflected from the substrate can be adequately detected by the VASE system. In the first film preparation run, the films spin-coated on silicon were too thick, especially for the blend samples that include the high molecular weight polymer material (Figure 4.11). To account for this, the solutions were diluted by adding 100 μL of chloroform to the already prepared solution. By reducing the solution concentration, all films were less than 80 nm thick, which made accurate ellipsometry measurements with depolarisation below the threshold for reasonable modelling possible. The following parameters determine the limits of applicability of ellipsometry measurements and are important considerations when preparing thin films of organic compounds for measurements:

Film Thickness — The film thickness should ideally be roughly equivalent to the wavelength of light used for the measurement. Films that are too highly absorbing (typically as a result of being too thick or heavily scattering) have a small light penetration depth so electric field in the layer of interest is damped too strongly.[82] Materials used for OPV devices are designed to be strongly absorbing and so films cast for ellipsometry must be 30-50% of the thickness of a film cast for a device ($\sim$30-80 nm).

Film Roughness — Ellipsometry works most effectively when the film roughness has an average height <10% of the probe beam wavelength. Larger features result in non-specular scattering of the incident beam and yields a depolarised reflected beam. This issue is accentuated as the angle of the ellipsometer relative to the plane of the film is made more acute.

Film Uniformity — Ideally, a film should have a uniform thickness across the measured region, otherwise the assumption of a parallel surface interface is no longer valid. Beam depolarisation measurements can be taken to quantify the degree to which a given incident beam is non-specularly scattered by the film due to surface irregularities.

When performing ellipsometry measurements, it is important to keep in mind that the data gathered will be very precise, however specifying the accuracy of an ellipsometer to an order of magnitude
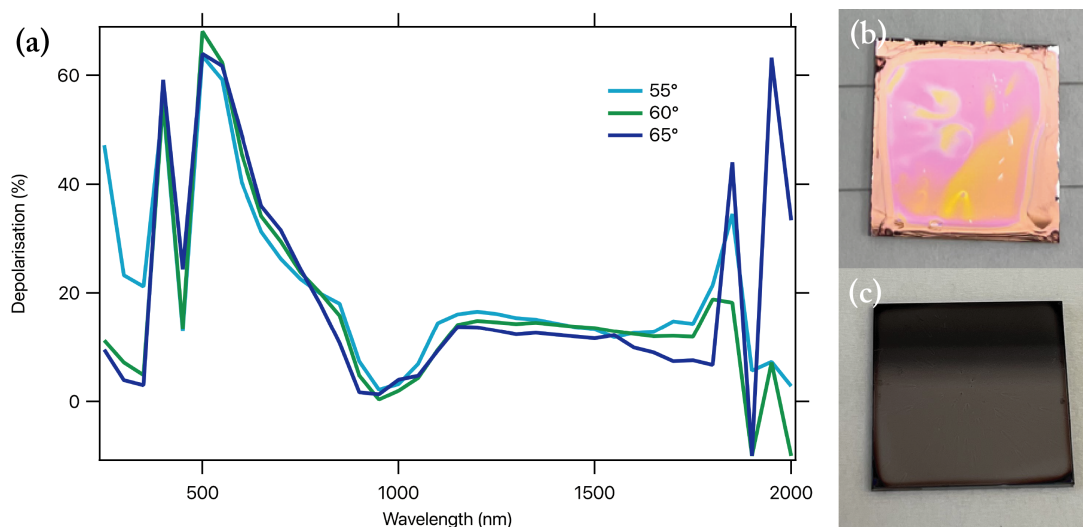
Figure 4.11: It is possible to measure the degree of depolarisation for light incident on the sample from the ellipsometer. (a) The high depolarisation at shorter wavelengths that occurs when measuring (b) is present as the film is too thick (i.e., too highly absorbing) and the change in colouration across the surface indicates that there are regions of varying thickness. (c) This sample of the same material blend was fabricated after the solution was diluted while retaining the same spin-coating conditions. The film quality is visibly more homogenous and provided a far more reliable measurement that could be used to perform optical modelling.

equivalent to the precision is nearly impossible. Ellipsometry will only provide data as good as the samples that are prepared and so one must take care in this first step to fabricate thin-films that have few visible imperfections.

> "Ellipsometry is perhaps the most surface sensitive technique in the universe. However you often don't know what it is you have measured so sensitively."[82]
> —*Eugene A. Irene*

4.3.1.3 Modelling with ellipsometry data

All experiments performed with the ellipsometry system never directly measure the parameters of interest but instead measure a quantity that is a function of these parameters.[82] This means that to make use of the data gathered from ellipsometry measurements, the measured data must be modelled to estimate the relevant function parameters that yield a resulting model that best fits the original measured data. By gathering data on polarisation states as a function of light beam wavelength, angle of incidence and polarisation state, it is possible to deduce physical characteristics of the sample.

Data collected from ellipsometry measurements can be used to create a model in WVASE to calculate the physical characteristics of interest. The model is built by first specifying the layers of the sample, starting with the silicon substrate and the natural oxide layer. Using a blank substrate, the thickness of this silicon oxide layer (typically on the order of ~3 nm) can be determined and then used for each of the subsequent thin-film samples. To model the wavelength-dependent optical properties of the organic layer, a Cauchy dispersion parameterisation was used. The default Cauchy dispersion model layer has six parameters, which are denoted in WVASE as the fitting constants A, B, C, the amplitude of the extinction coefficient α, an exponential factor β and the band edge γ. All bar the final parameter

Cauchy	~30-80nm
SiO$_2$	~3nm
Si Wafer	~1mm

FIGURE 4.12: The modelling layers used when analysing ellipsometry data for organic thin films with WVASE. Coloured labels indicate that the software is used to model the physical parameters of the film.

can be set as a variable fit parameter.[84] The parameters are related to the optical constants n and k via,

$$n(\lambda) = A + \frac{B}{\lambda^2} + \frac{C}{\lambda^4}, \tag{4.6}$$

and,

$$k(\lambda) = \alpha \exp \beta (12400(\frac{1}{\lambda}) - \frac{1}{\gamma}). \tag{4.7}$$

First, it was necessary to fit A, B and C using the ellipsometry data for the transparent region of the organic film and the iterative Marquardt-Levenberg fitting algorithm to approximate the organic film thickness (Figure 4.12).[84] This approach is a damped, non-linear fitting method that uses all the data within the selected range to provide a least-squares fit as long as the thin-film data for the various angle measurements follows a regular pattern. Once this is complete and the *mean squared error* (MSE) of the fit is ≤ 2, it is the necessary to check the physical reasonableness of the fit by looking at the calculated refractive index and extinction coefficient of the transparent range. The refractive index should follow an exponential decay as wavelength increases and the extinction coefficient should be zero (as silicon is optically transparent in the infrared). Using a Dektak profilometer, it was possible to corroborate the film thickness approximated with optical modelling.

Once this initial process was complete, it was then possible to use data from the complete wavelength range to perform a point-by-point fit that works with the data in wavelength steps. At each wavelength, the same parameters that would end a normal fit progress the point-by-point fit to the next step (i.e., MSE lower than the absolute lower limit). In this instance, the layer thickness and the parameters from Equation 4.6 were held constant to determine the optical constants at each wavelength.

Once the fitting was complete, the next step was to check the optical constants n and k plotted against wavelength to check for excessive noise in the fit or unusual features including points within the visible range where $k = 0$. If any issues were apparent, the fit was redone by first restricting the wavelength or angle range produced as a result of an overly shallow angle of incidence or issues with the film quality at the edges (Figure 4.13). If the peaks of k appear to fit the peaks of the measured thin-film absorption spectra well, the data was then transferred to MATLAB where it can be converted using,

$$a = \frac{4\pi k}{\lambda}, \tag{4.8}$$

into an absorption spectra before being plotted to compare with the absorption spectra recorded using UV-Vis spectroscopy. WVASE applies 90% confidence limits on fits using this approach.

At this point in the modelling process, if the absorption spectra fit was reasonable, the next task was to calculate the high-frequency dielectric constant which can be determined using,

$$\kappa = n^2, \tag{4.9}$$

by taking the mean of the values for $n(\lambda)$ in the transparent region (neglecting regions that are overly noisy, especially towards the infrared range). This relation arises as a result of the manipulation of Maxwell's equations which describe the speed of light in a vacuum,

$$c = (\mu_0 \varepsilon_0)^{-\frac{1}{2}}, \tag{4.10}$$

where for a diamagnetic material it can be stated that,

$$c_m = (\mu_0 \varepsilon)^{-\frac{1}{2}}. \tag{4.11}$$

The refractive index can then be expressed in terms of ε and μ,

$$n = \left(\frac{\mu_0 \varepsilon_0}{\mu_0 \varepsilon} \right)^{-\frac{1}{2}}, \tag{4.12}$$

which can be simplified to,

$$n = \left(\frac{\varepsilon}{\varepsilon_0} \right)^{-\frac{1}{2}}. \tag{4.13}$$

The dielectric constant is then defined by,

$$\kappa = \frac{\varepsilon}{\varepsilon_0}, \tag{4.14}$$

and so Equation 4.13 can be rewritten in the desired form,

$$\kappa = n^2. \tag{4.15}$$

In an OPV device, increasing the dielectric constant is seen as a path towards reduced exciton binding energy, reduced Coulombic attraction for the CT state and an overall reduction in exciton recombination.[83] As will be discussed further in the next chapter, altering the concentration of donor polymer with respect to the acceptor small molecule can produce measurable changes in the dielectric constant of the thin-film that will subsequently have an impact on OPV device performance.

| Ellipsometric measurements | → | Modelling of polarisation transformation coefficients | → | Fitting paramaters of interest with optical modelling | → | Physical parameters of thin film are outputted |
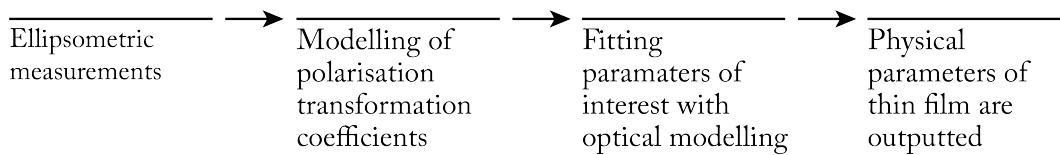
FIGURE 4.13: The generalised workflow for modelling and fitting ellipsometry data.

4.3.2 Quantifying the absorption spectra

The absorption spectra were measured with a Varian Cary 5000 spectrometer that uses a deuterium arc UV-range source and tungsten halogen visible-range bulb to illuminate the thin-film.[85] A single channel photon detection system measures the intensity of the transmitted light to a high degree of precision, where transmittance (T) is related to absorbance (A) by,

$$A = -\log_{10} T.^{[85,86]} \tag{4.16}$$

(a)

(b)
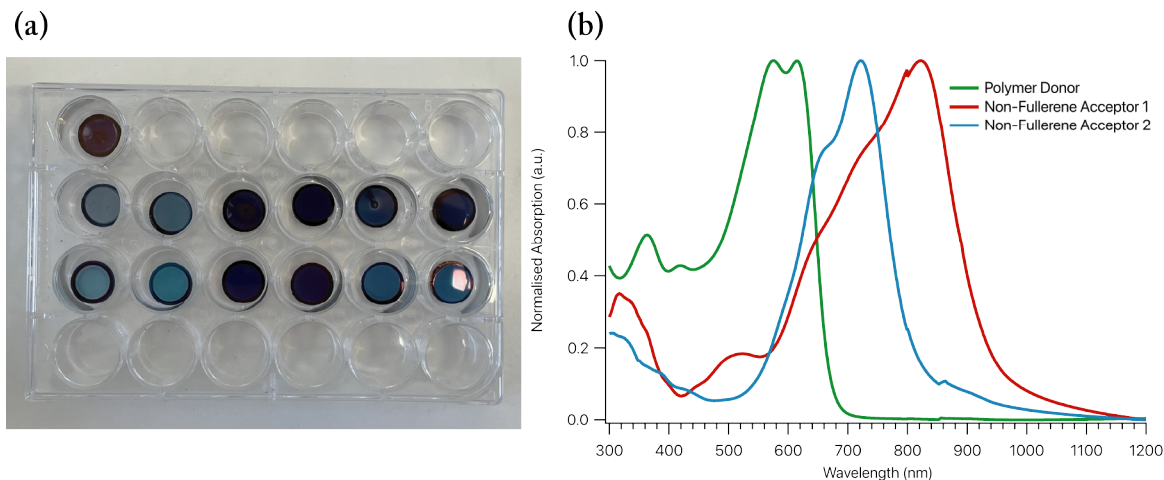
FIGURE 4.14: (a) Fused silica samples of neat and blend films prepared for absorption spectra measurements. (b) Example absorption spectra for neat films for both donor and acceptor materials where this particular donor absorbs most strongly at shorter wavelengths.

Samples for absorption spectra measurements were prepared on fused silica substrates. Solutions of neat PM6, Y6 and ITIC-2F were prepared in chloroform with total concentrations of 9 mg/mL. Blend solutions of PM6:ITIC-2F and PM6:Y6 were prepared in chloroform with total concentrations of 16-18 mg/mL. All samples were spin-coated at 3000 rpm for 30 seconds before the blend films were subsequently annealed at 110 °C for 10 minutes in a nitrogen filled glovebox. Neat films were left as-cast.

The absorbances for these materials were calculated using,

$$A = \frac{\alpha \ln 10}{d}, \tag{4.17}$$

where α is the absorption coefficient measured by the spectrometer and d is the thickness of the sample measured in centimetres. As the absorbance is scaled by the film thickness, it is a measure of the light absorption properties of the materials used to fabricate the thin-film.

4.3.3 Determining film density

XRR was used to determine the physical characteristics of thin-films using short wavelength radiation at varying angles around the angle of total internal reflection. By performing measurements above and below the critical angle (at or below which total internal reflection of the beam will occur), the intensity of the partially reflected X-ray beam can be measured (Figure 4.15).[87] To a first approximation, the scattering intensity is proportional to the square of the absolute value of the Fourier transform of the film's electron density.[87] Modelling this interference pattern using computational methods, enables the calculation of parameters such as the thin-film thickness, density and surface roughness for films that are monocrystalline, polycrystalline or amorphous (a majority of solution processed thin films fall into this final category). The film thickness can be calculated using the periodicity of oscillations, while the angular dependency of the oscillation amplitude can be used to determine the surface and interface roughness.

As with other optical techniques (including ellipsometry), measurement difficulties can be expected with highly-absorbing or strongly-scattering films and so the films produced on silicon for XRR should

be quite thin (30-80 nm). For the measurements performed as part of this research programme, the same samples used for ellipsometry were also used for XRR.
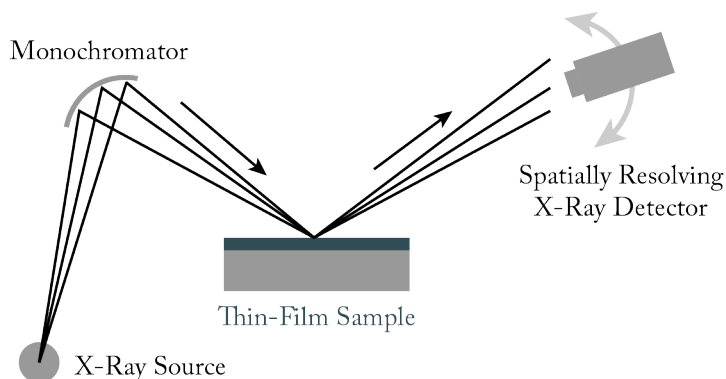
FIGURE 4.15: A simplified schematic of the instrument used to perform XRR measurements. The stationary X-ray source emits a beam (in our case, a copper source that emits radiation at a wavelength of 1.54 Å) that passes through a monochromator that is aligned with the sample stage. The beam incident on the sample is reflected near the angle of total internal reflection and is detected by a moving X-ray detection system. [88]
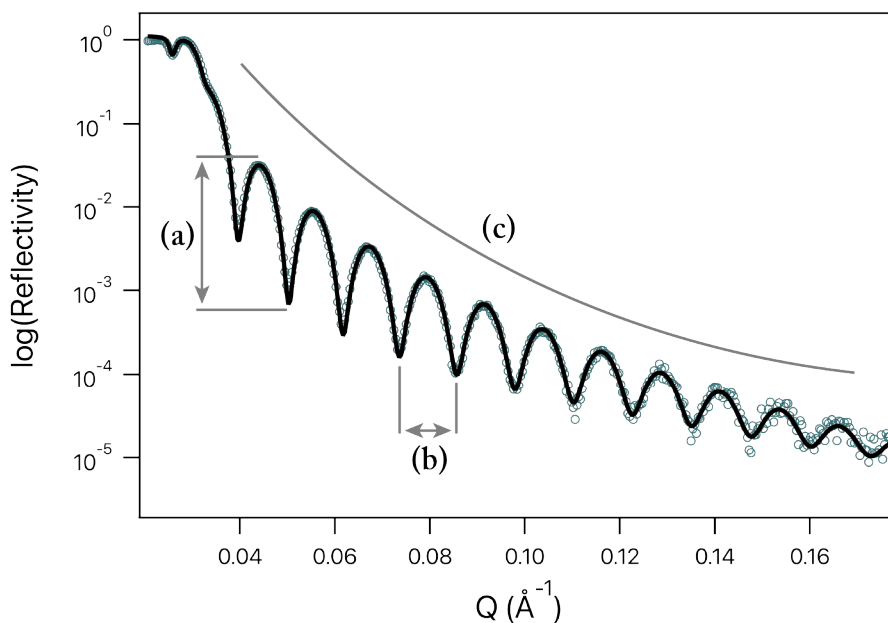
FIGURE 4.16: An XRR reflectometry profile produced of an organic thin-film spin-coated on a silicon substrate. The log of the magnitude of reflected beam intensity is plotted with respect to the measurement angle- and wavelength-dependent wave-vector Q. (a) The scattering length density of the film is defined by critical angle which is represented by the initial drop in signal intensity, (b) thickness by the fringe separation and (c) surface roughness by the decay of the fringe amplitude. A greater contrast in electron density between layers will result in larger fringe signal amplitudes. [89]

    Using the open source software package `Motofit` within the `IGOR Pro` environment, it is possible to model X-ray reflectivity data and determine the physical characteristics noted above. XRR data

collection and modelling was performed by Ronan Chu at COPE and provided important insights into the thin film density.

4.3.4 Measuring film surface topology

AFM was used to study the surface topology of active layer films. The high resolution (over 1000 times better than the Abbe optical diffraction limit) and ability to directly manipulate the sample using the detection probe make AFM incredibly powerful technique with a broad array of applications. It is important to recognise the key limitation of this materials analysis technique, that is, it can only be used to study the surface of a thin-film, unlike optical techniques such as ellipsometry and XRR that can be used to study the bulk morphology. In this low donor content study, AFM served the specific purpose of studying the affect that altering the polymer content of the thin-films had on surface roughness. Increasing the polymer content of an active layer blend typically reduced the surface roughness, which is advantageous for the formation of a pore-free contact between the active layer and charge transport layer.

4.3.4.1 Fundamental working principle

Atomic force microscopy (AFM) uses a probe with a radius of 2 to 50 nm to scan over the surface of a sample. When used in peak force tapping mode, the probe is attached at the end of a cantilever that is driven at a resonant frequency such that it periodically interacts with the sample surface with an oscillation amplitude on the order of 10 to 100 nm. The oscillation frequency and amplitude of this oscillation will change when the probe is brought close to the sample due to Van der Waals forces and dipole-dipole interactions. By measuring the degree of probe deflection it is possible to produce a topography of the sample surface.

4.3.4.2 Sample Preparation

AFM samples with a Y6-based active layer were prepared with a conventional structure of ITO/PE-DOT:PSS/PM6:Y6 to leave the top surface of the active layer exposed for measurement. The ITO sputter-coated glass substrates were pre-processed with the wet and dry cleaning method described in Section 4.2. PEDOT:PSS was spin-coated on the cleaned ITO substrates at 5000 rpm for 30 seconds, followed by annealing at 150 °C for 15 minutes in air to produce a 10 nm HTL. Next, neat Y6 and PM6:Y6 blends in the two donor concentrations were dissolved in chloroform so as to produce total concentrations of 16-18 mg/mL. The solutions were left to mix for two hours at 60 °C. The solutions were then spin-coated at 5000 rpm to produce 120 nm thick active layers that were then thermally annealed at 110 °C for 10 minutes in the glovebox.

4.3.4.3 Measurement Process

In this research programme, a Bruker Dimension XR system capable of peak force tapping mode AFM was used to analyse the sample surfaces. Tapping mode AFM is designed as a compromise between having the probe close enough to the sample such that interaction forces can be accurately measured while avoiding the issue that is frequently encountered with contact mode AFM where the probe becomes lodged on the surface of the sample. The Bruker system automatically controls the tapping oscillation force and frequency depending on the characteristics of the surface being measured.[90] This further simplifies the data acquisition process by removing the need to manually tune the tapping mode oscillation frequency and amplitude to achieve good image quality and avoid damage to the probe.

OPV devices based on NFA materials have achieved significant gains in performance over the past decade as a result of the myriad benefits that arise from the ability to precisely alter the structural properties of these compounds. In most prior studies of OPV devices, the key parameters for minimising losses due to non-Langevin recombination are balanced charge mobility and morphology. To achieve this, it was the dominant assumption that a continuous interpenetrating network of donor and acceptor (i.e., a bulk heterojunction with a balanced ratio of donor and acceptor materials) was necessary to produce the interfacial area required for efficient exciton dissociation and high free charge mobility. In a typical low donor content device, it might be expected that the increasing distance between donor-rich domains leads to a greater probability of recombination as a result of unbalanced charge transport efficiencies.[91] The focus of this research programme was to investigate the affect of reducing the donor content in active layer blends on OPV device performance. Two structurally distinct, high-performance NFA acceptor materials blended with the same donor polymer material were compared. The outlook and perspectives on future work that arise from the results presented below are discussed in the following chapter.

5.1   OPV Devices

5.1.1   Device Fabrication

The first stage of this research programme focussed on the fabrication and testing of complete OPV devices. All materials used in device fabrication were acquired from commercial suppliers, as listed in Section 4.1. The optimised blend ratios for the best performing devices using both Y6 and ITIC-2F were sourced from literature.[52,63] In the case of PM6:ITIC-2F blends, optimised device performance has been achieved from a 1:1 weight ratio blend fabricated in an inverted structure. As for PM6:Y6, a slightly higher concentration of acceptor to produce a 1:1.2 weight ratio in a conventional structure device was reported as having delivered the highest PCE.

As described in Chapter 4, the fabrication process follows a set procedure with variations for whether the device has been fabricated with a conventional or inverted structure. In a conventional device, PEDOT:PSS is used to modify the work function of the ITO layer and ensure closer to Ohmic contact with the active layer. As presented in Figure 4.2, both conventional and inverted device architectures were investigated. It was found that, for particular active layer blends, either a conventional

or inverted structure delivered better photovoltaic performance and so both structures are typically tri-
alled during the performance optimisation process. All devices produced for this research programme
were fabricated and tested on the same day so as to minimise exposure to air and avoid degradation.
As described in the following section, thermal annealing was used as a post-processing step for almost
all solution-processed devices during fabrication. In the context of active layer fabrication, thermal
annealing enables the reorganisation of molecules that can result in improved device performance.

5.1.1.1 Y6-based Devices

OPV devices with a Y6-based active layer were prepared with a conventional structure of ITO/PE-
DOT:PSS/PM6:Y6/PDINO/Ag. The ITO sputter-coated glass substrates were pre-processed with
the wet and dry cleaning method described in Section 4.2. PEDOT:PSS was spin-coated on the
cleaned ITO substrates at 5000 rpm for 30 seconds, followed by annealing at 150 °C for 15 minutes
in air to produce a 10 nm HTL. Next, PM6:Y6 in the two donor concentrations were dissolved in
chloroform so as to produce total concentrations of 16-18 mg/mL. The active layer blends were left to
mix for two hours at 60 °C to ensure complete dissolution of the donor and acceptor materials in the
solvent. The active layers blends were then spin-coated at 5000 rpm to produce 120 nm thick active
layers that were then thermally annealed at 110 °C for 10 minutes in the glovebox. In the case of the
thicker, 200 nm active layer devices, a spin-speed of 3000 rpm was used with the same post-processing
annealing step. PDINO (prepared as a 1.5 mg/mL dilution in methanol) was then spin-coated on
the annealed active layers at 3000 rpm to form the ETL layer with a thickness of 10 nm. Finally,
silver was thermally evaporated to a thickness of 100 nm through a shadow mask under high vacuum
(1×10^{-6} bar) to produce the capping electrode. The effective area of the devices, as defined by the
shadow mask area, was 0.08 cm^2. The thickness of the active layer is a critical parameter when seeking
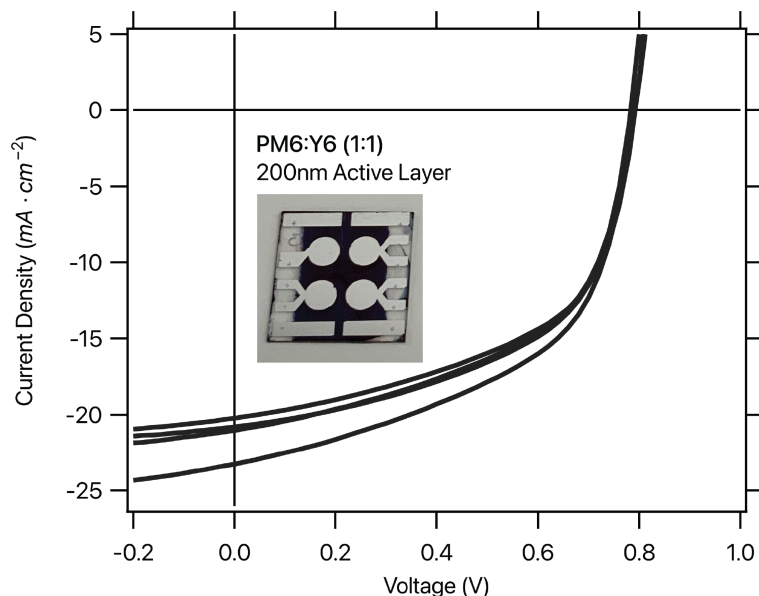
FIGURE 5.1: Typical current density-voltage curves for PM6:Y6 OPV devices fabricated with the
thicker 200nm active layer. Inset, a PM6:Y6 (1:1.2) device.

to optimise overall device performance. While devices using a blend of PM6:Y6 have been shown to
maintain strong performance even with active layer thicknesses of over 300 nm, the best performance
can be achieved with an active layer 100-125 nm thick. Active layers fabricated within this thickness

Table 5.1: PM6:Y6 Device Performance with 200nm Active Layer

W. Ratio	J_{SC}	V_{OC}	FF	PCE	Best PCE
w/w	(mA/cm^2)	(V)		(%)	(%)
1:1.2	21.3±0.9	0.78±0.01	0.54±0.02	9.0±0.5	9.6

range tend to have the best balance of light absorption and charge extraction efficiencies. During the fabrication optimisation process for the PM6:Y6 devices, a thicker active layer of approximately 200 nm was trialled by retaining the blend solution concentration and reducing the spin speed. While J_{SC} was comparable to the devices fabricated with active layers within the optimum range, the V_{OC} was approximately 20% greater for these thicker-junction devices which is closer to the acceptor LUMO to donor HOMO offset of PM6:Y6 of 1.4 eV (Table 5.1).[92] Overall PCE is reduced for these devices, however, as the FF is approximately 10% lower than for the devices with optimised active layer thicknesses which is a result of reduced charge extraction efficiency. As active layer thickness increases, the probability of free charge recombination increases as the distance from the site of exciton dissociation to the charge transport layers increases.

5.1.1.2 ITIC-2F-based Devices

OPV devices with an ITIC-2F-based active layer were prepared with an inverted structure of ITO/ZnO/ PM6:ITIC-2F/MoOx/Ag. The ITO sputter-coated glass substrates were pre-processed with the wet and dry cleaning method described in Section 4.2. A zinc oxide precursor solution (prepared as a 1:7 volume dilution of diethylzinc dissolved in hexane in tetrahydrofuran) was spin-coated on the cleaned ITO substrates at 1500 rpm for 30 seconds in the glovebox, followed by annealing at 150 °C for 15 minutes in air to produce a 10 nm zinc oxide ETL. Next, PM6:ITIC-2F in the two ratios were dissolved in chloroform so as to produce total concentrations of 16-18 mg/mL. The active layer blend solutions were left to mix for two hours at 60 °C to ensure complete dissolution of the donor and acceptor materials in the solvent. The active layers blends were then spin-coated at 5000 rpm to produce 120 nm thick active layers that were then thermally annealed at 110 °C for 10 minutes in the glovebox. Molybdenum oxide was then thermally evaporated to a thickness of 10 nm through a shadow mask under high vacuum (1×10^{-6} bar) to form the HTL layer with a thickness of 10 nm. Finally, silver was thermally evaporated to a thickness of 100 nm using the same method. The effective area of the devices, as defined by the shadow mask area, was again 0.08 cm^2.

5.1.2 Performance Analysis

At initial inspection, both the PM6:Y6 and PM6:ITIC-2F devices delivered strong photovoltaic performance for both blend weight ratios tested. The best PM6:Y6 devices with 1:1.2 and 1:8 weight blends gave comparable performance statistics with a similar trend apparent with the best PM6:ITIC-2F based devices. Despite the similarities between measured V_{OC} for both PM6:Y6 and PM6:ITIC-2F devices, there is a clear difference in overall device performance for these two NFAs. Independent of the blend ratio, ITIC-2F-based devices had lower J_{SC}s and FFs compared with Y6-based devices, leading to a lower PCE. The following sections will describe how these results were contextualised in terms of the light absorption properties of the devices containing these NFA materials and their morphological properties.

In an ideal OPV device, the V_{OC} approaches the offset of the donor HOMO and acceptor LUMO energies. In practise, V_{OC} also depends on the CT-state energy at the donor-acceptor interface and the CT-state decay rate rather than that of free charges. At V_{OC}, all photogenerated charge carriers

recombine. This means that V_{OC} depends not only on the HOMO-LUMO levels of the materials but also the recombination kinetics. A maximum V_{OC} will be achieved for a given active layer blend when radiative decay of strongly absorbing exciton states is the dominant recombination pathway. As a point of comparison between the PM6:Y6 and PM6:ITIC-2F devices, both blends have very similar donor HOMO to acceptor LUMO offsets and exhibit similar V_{OC}s (within experimental uncertainty) across all device blends. This suggests that the CT-state energy for both donor-acceptor blends are quite similar.

For PM6:ITIC-2F devices, it was noted that both blend ratios exhibit quite low FF. As discussed in Section 4.2.2 FF is highly sensitive to bulk morphology and the efficiency of charge extraction after exciton dissociation. As both the 1:1 and 1:8 devices exhibit low FFs, these results can be attributed to high rates of free charge recombination due to the amorphous structure of these blends. FF is also highly dependent on the thickness of the active layer. The PM6:Y6 (1:1.2) devices exhibit a lower average FF of 0.54 ± 0.02 when compared with PM6:Y6 devices with optimised active layers that have an average FF of 0.65 ± 0.01 (Table 5.1). This drop in FF can be attributed to an increase in recombinative losses as separated charges now travel further on average to reach the charge transport layers for devices with thicker active layers. In the case of the PM6:Y6 (1:1.2) devices, their greater FFs may in part be due to the higher degree of structural ordering observed in the active layers produced using these blends, as discussed in Section 5.3.2.
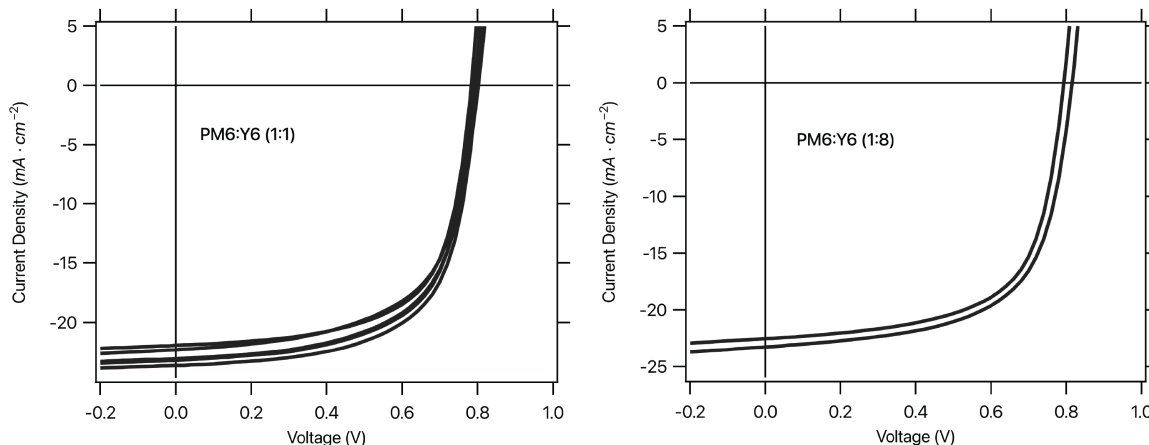
FIGURE 5.2: Current density-voltage curves for the best performing pixels fabricated with PM6:Y6 blends. All devices for each material combination and blend ratio were fabricated at the same time under the same processing conditions.

Table 5.2: PM6:Y6 Optimised Device Performance

W. Ratio	J_{SC}	V_{OC}	FF	PCE	Best PCE
w/w	(mA/cm^2)	(V)		(%)	(%)
1:1.2	21.9 ± 0.6	0.79 ± 0.01	0.65 ± 0.01	11.1 ± 0.7	12.2
1:8	22.8 ± 0.5	0.73 ± 0.07	0.60 ± 0.04	11.9 ± 0.1	11.9
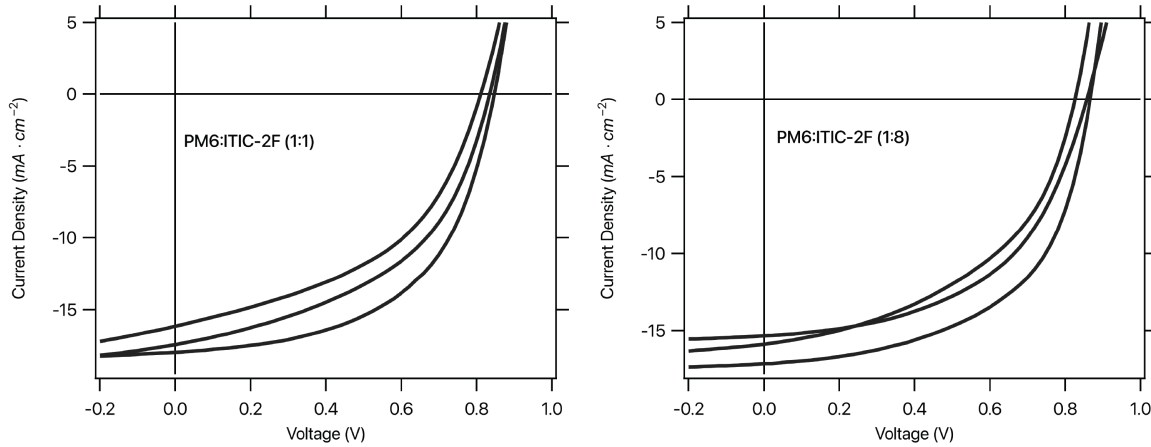
FIGURE 5.3: Current density-voltage curves for the best performing pixels fabricated with PM6:ITIC-2F blends. All devices for each material combination and blend ratio were fabricated at the same time under the same processing conditions.

Table 5.3: PM6:ITIC-2F Optimised Device Performance

W. Ratio	J_{SC}	V_{OC}	FF	PCE	Best PCE
w/w	(mA/cm^2)	(V)		(%)	(%)
1:1	17.2±0.3	0.80±0.03	0.47±0.05	6.6±1.1	8.3
1:8	15.8±0.3	0.83±0.02	0.51±0.04	6.8±0.9	8.2

Measuring the device EQE gives an indication of the charge generation efficiency with respect to the intensity of absorbed light and can be integrated to calculate J_{SC}. The EQE spectra of the best two PM6:Y6 (1:1.2 weight ratio) devices shown in Figure 5.4 demonstrate that the maximum EQE plateau reached approximately 55% to 65% from 450 nm to 830 nm with an integrated J_{SC} of 21.0 mA/cm^2 and 19.2 mA/cm^2. This result agrees quite well with the J_{SC} value from the current density-voltage curve within a 9% mismatch.

When testing devices, it is also essential to assess their diode properties by performing dark current density-voltage measurements. Dark current density-voltage measurements can reveal the presence of charge loss pathways that occur as a result of defects with the device structure. With no photocurrent, the injected current is driven by diffusion against the built-in potential. [17] As expected given the strong device performance, the gradient of the dark current density-voltage curves for PM6:Y6 devices in Figure 5.5 match those of the light current density-voltage curves at higher voltages which is an indicator of good diode performance and minimal parasitic charge loss pathways. For the best PM6:ITIC-2F devices, it can be seen that the lower two plots show a mismatch in current density-voltage gradient for dark and light scans near 0.8 V, which is different to the PM6:Y6 devices. This shallower gradient for the dark current density-voltage curves at higher voltages indicates that there might be defects present in the active layer films such as pinholes that act as localised shunts (i.e., sites of current loss).

Data gathered from the current density-voltage measurements also reveal the series (R_{SE}) and shunt (R_{SH}) resistances of the OPV device, the former a limiting factor for V_{OC} and the latter a measure of the propensity for current losses to arise, which impacts overall photocurrent and, by extension, FF. Table 5.4 presents the R_{SE} and R_{SH} the best performing devices from each material blend and weight ratio. The best PM6:Y6 device (1:1.2 weight ratio) demonstrates an exceptionally low R_{SE} and high R_{SH}, with the latter an indicator that photocurrent loss due to parasitic leakage currents is minimal.
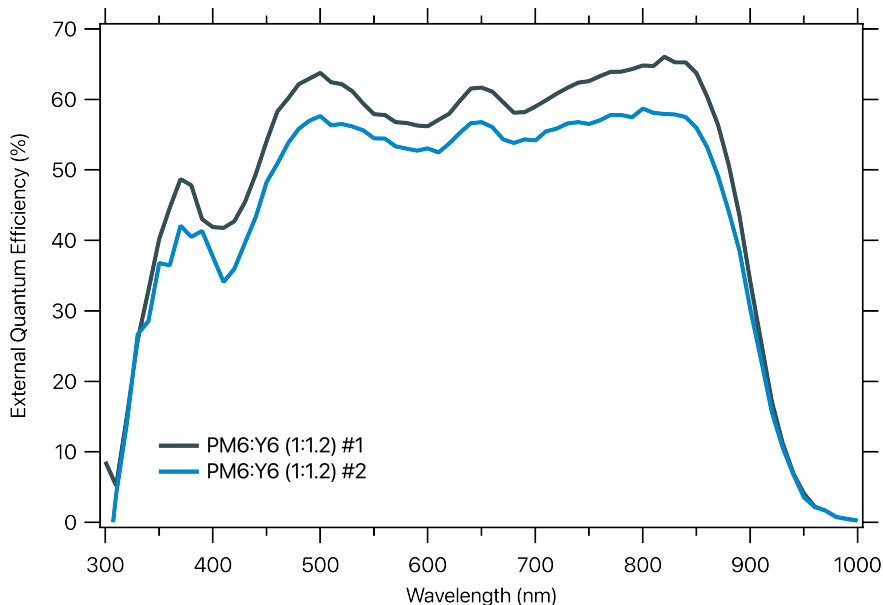
Figure 5.4: EQE curve for the best two PM6:Y6 devices.

Table 5.4: Device Series and Shunt Resistance

Blend	Weight Ratio	R_{SE}	R_{SH}
	w/w	Ω	Ω
PM6:ITIC-2F	1:1	125	6300
PM6:ITIC-2F	1.8	119	6900
PM6:Y6	1:1.2	67	9400
PM6:Y6	1:8	76	4500

5.2 Optical properties of the active layer

5.2.1 Absorption Characteristics

The absorption characteristics of the films were measured as a first step in the understanding the difference in performance between the devices containing the different NFA. The conjugated polymer PM6 was selected as the donor material for both Y6 and ITIC-2F devices. As demonstrated in Figure 5.6, PM6 has a medium optical gap ($E_{OPT} = 1.8$ eV) with a complementary absorption spectra absorbing at shorter wavelengths than the acceptors. The small LUMO offset between donor and acceptor materials would not be expected to provide the driving energy for exciton splitting, but it is important to take into account interfacial effects and exciton binding energy.[9] Balancing complementary absorption with minimised energy offsets between donor and acceptor is one of the key factors underpinning the strong photovoltaic performance of the two material blends trialled as part of this study. To enable comparisons across blend ratios and NFAs, all OPV devices were fabricated with the same active layer thickness. A consistent active layer thickness across OPV devices meant that, in the context of optical properties, changes in absorption were solely a result of differences in material characteristics and bulk morphology.

As discussed in Section 5.1.2, the J_{SC} was only marginally greater for PM6:Y6 devices with the 1:8 blend (22.8 ± 0.5 mA/cm^2) compared to the 1:1.2 blend (21.9 ± 0.5 mA/cm^2) and could be considered to be within experimental uncertainty. J_{SC} is, in part, related to the absorption characteristics
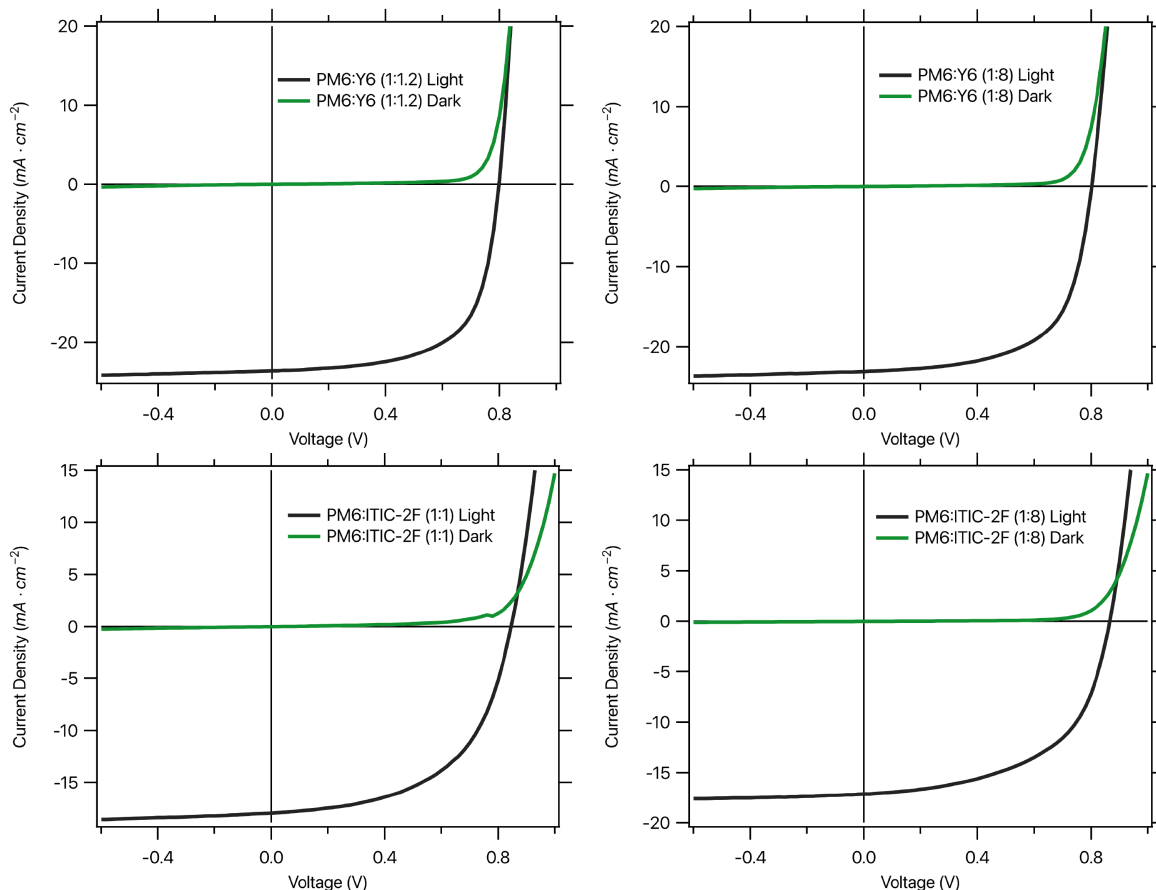
FIGURE 5.5: Dark and light current density-voltage curves from the best performing devices fabricated with blends of PM6:ITIC-2F and PM6:Y6 in the two weight ratios.

of the materials used in the active layer blend. The integrated absorbance of the 1:8 blend film is only marginally greater ($\sim$8%) than that of the 1:1.2 blend film, indicating that the light absorption characteristics of the active layers are very similar independent of the donor content. In the case of PM6:ITIC-2F devices, 1:1 weight blend devices demonstrated a higher J_{SC} (17.2 $\pm$ 0.3 mA/cm^2) than the 1:8 blend devices (15.8 $\pm$ 0.3 mA/cm^2). The integrated absorbance for the 1:8 blend film was $\sim$12% greater than that of the 1:1 blend, indicating that this change in J_{SC} was most likely not a result of reduced light absorption efficiency.

Directly comparing the PM6:Y6 and PM6:ITIC-2F active layers, regardless of blend weight ratio, J_{SC} was consistently greater for devices fabricated with the Y6-based blends. Comparing the absorbance characteristics of the two blend types, blends of PM6:Y6 demonstrated an integrated absorption only 5% greater than that of PM6:ITIC-2F. As the light absorption characteristics of both NFA materials are so similar, the observed difference in J_{SC} should therefore be attributed to another property of these active layers. J_{SC}, as with each of the metrics presented for device performance, is not solely a measure of absorption efficiency and incorporates other aspects of device performance. For instance, changes in J_{SC} will occur as a result of differences in exciton diffusion lengths. In the case of the PM6:ITIC-2F devices, reduced interfacial surface area between donor and acceptor can lead to a higher probability of the exciton decaying due to the longer average path length required for the exciton to diffuse to an interface.

'

Table 5.5: Absorption Spectra Sample Thickness

Blend	Weight Ratio	Film Thickness
	w/w	nm
PM6	-	450±45
ITIC-2F	-	85±8
PM6:ITIC-2F	1:1	240±24
PM6:ITIC-2F	1.8	110±11
Y6	-	60±6
PM6:Y6	1:1.2	240±24
PM6:Y6	1:8	155±15
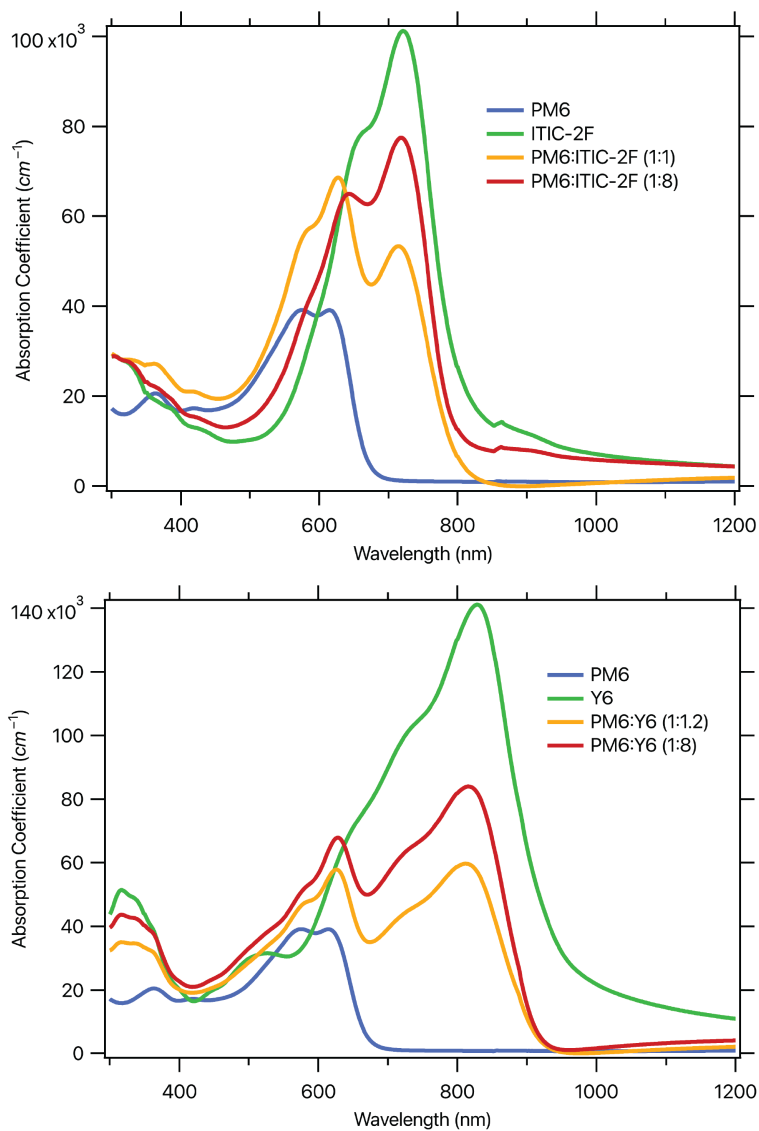
FIGURE 5.6: Absorption coefficients for PM6, ITIC-2F, Y6 and blends of these materials.
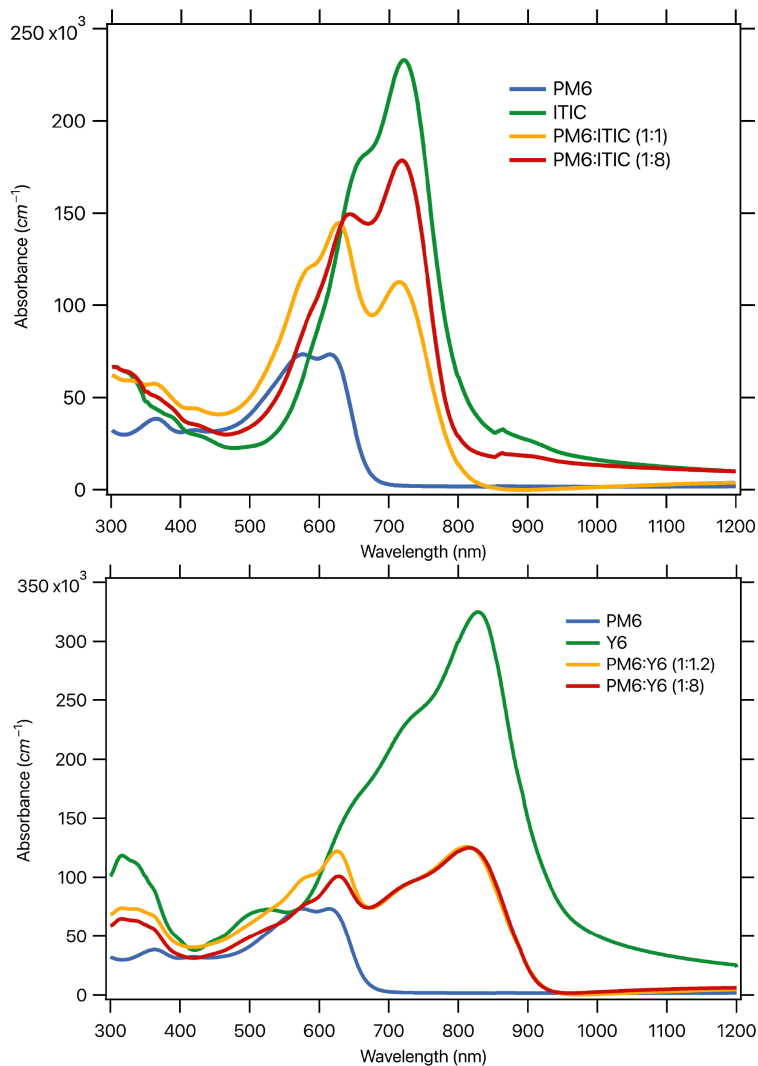
FIGURE 5.7: Calculated absorbance for PM6, ITIC-2F, Y6 and blends of these materials.

5.2.2 Film Optical Properties

Optical modelling performed using the VASE data for each of the neat materials and blends containing them provided further insight into their optical properties. Maximising the extinction coefficient across a broad wavelength range correlates with an enhanced probability of exciton generation for a given thickness. Given the very strong absorbance of Y6 demonstrated in the previous section, it can be seen in Figure 5.8 the extinction coefficient of the neat film is very high across the region of peak absorption. As PM6 content is increased in the Y6 blend films, a slight increase in the extinction coefficient in the 400-700 nm wavelength range of the donor material is observed in Figure 5.8, along with a decrease in the peak refractive index.

Neat and blended films with ITIC-2F exhibited lower extinction coefficients compared with Y6-based films which correlates with the results presented for absorbance and J_{SC} for complete devices. The effect of increased PM6 content is also more apparent for the PM6:ITIC-2F blends compared with the PM6:Y6 blends. Figure 5.8 demonstrates significantly increased extinction coefficients of both PM6:ITIC-2F blends within the 400-700 nm range compared with the ITIC-2F neat film. For

both Y6- and ITIC-2F-based blends, the benefit of blending a donor material with complementary light absorption characteristics is clear as broadening the absorption range is essential for optimal OPV device performance.

When the donor content is reduced in the 1:8 blends for both acceptor materials, their optical properties remain very similar to those of the optimised blends. From the perspective of film optical properties, reducing the donor content is not expected to significantly impact the overall light absorption and exciton generation efficiency of low donor content devices. As discussed in Section 5.2.1, J_{SC} is similar when comparing the two weight ratios for each NFA blend which aligns with this observation.

Applying the Cauchy modelling technique described in Section 4.3.1, one of the best visual indicators of its effectiveness can be found in the transparent region of the sample (i.e., above 1300 nm). In this region, k should be zero as no light absorption is occurring. Some of the models presented for the extinction coefficient in Figure 5.8 (black lines) have non-zero values for k in the transparent region even after a process of model optimisation. As all the sample films had a uniform surface and were less than 100 nm thick, this result is most likely a result of anisotropy within the bulk of the film. Ellipsometry measurements can be considered to be taken from an average across the sample. As a result, our ability to discern the precise morphological properties of the film from the optical properties are limited, particularly if the films are highly anisotropic. Performing measurements of the bulk morphology to understand the packing characteristics of the donor and acceptor molecules can give greater context to these results.

Table 5.6: PM6:Y6 Blend Dielectric Constants

Blend	Weight Ratio	Refractive Index	Dielectric Constant	Film Thickness
	w/w	n	ε	nm (modelled)
Neat PM6	-	1.84±0.09	3.38±0.33	68±6
Neat Y6	-	2.13±0.10	4.53±0.43	80±8
PM6:Y6	1:1.2	2.06±0.10	4.24±0.41	52±5
PM6:Y6	1:8	2.12±0.10	4.49±0.42	53±5

Table 5.7: PM6:Y6 Blend Dielectric Constants

Blend	Weight Ratio	Refractive Index	Dielectric Constant	Film Thickness
	w/w	n	ε	nm (modelled)
Neat PM6	-	1.84±0.09	3.38±0.33	68±6
Neat ITIC-2F	-	1.88±0.09	3.53±0.33	73±7
PM6:ITIC-2F	1:1	1.85±0.09	3.42±0.33	65±6
PM6:ITIC-2F	1:8	1.84±0.09	3.38±0.33	47±4

As discussed in Section 4.3.1, the dielectric constant provides an indication of the ability of the material to screen charges (i.e., its polarisability).[17] The greater the dielectric constant, the higher the polarisability, which may be beneficial in the context of OPV devices as this has been postulated to lead to a reduced exciton binding energy.

Y6 features a uniquely high optical frequency dielectric constant for an organic semiconducting material ($\varepsilon = 4.53$) and so the blends made from it also exhibited particularly strong dielectric constants that correlate with their high overall device performance. As Y6 content of these blends was reduced through the addition of the donor material, the dielectric constant reduced marginally. The
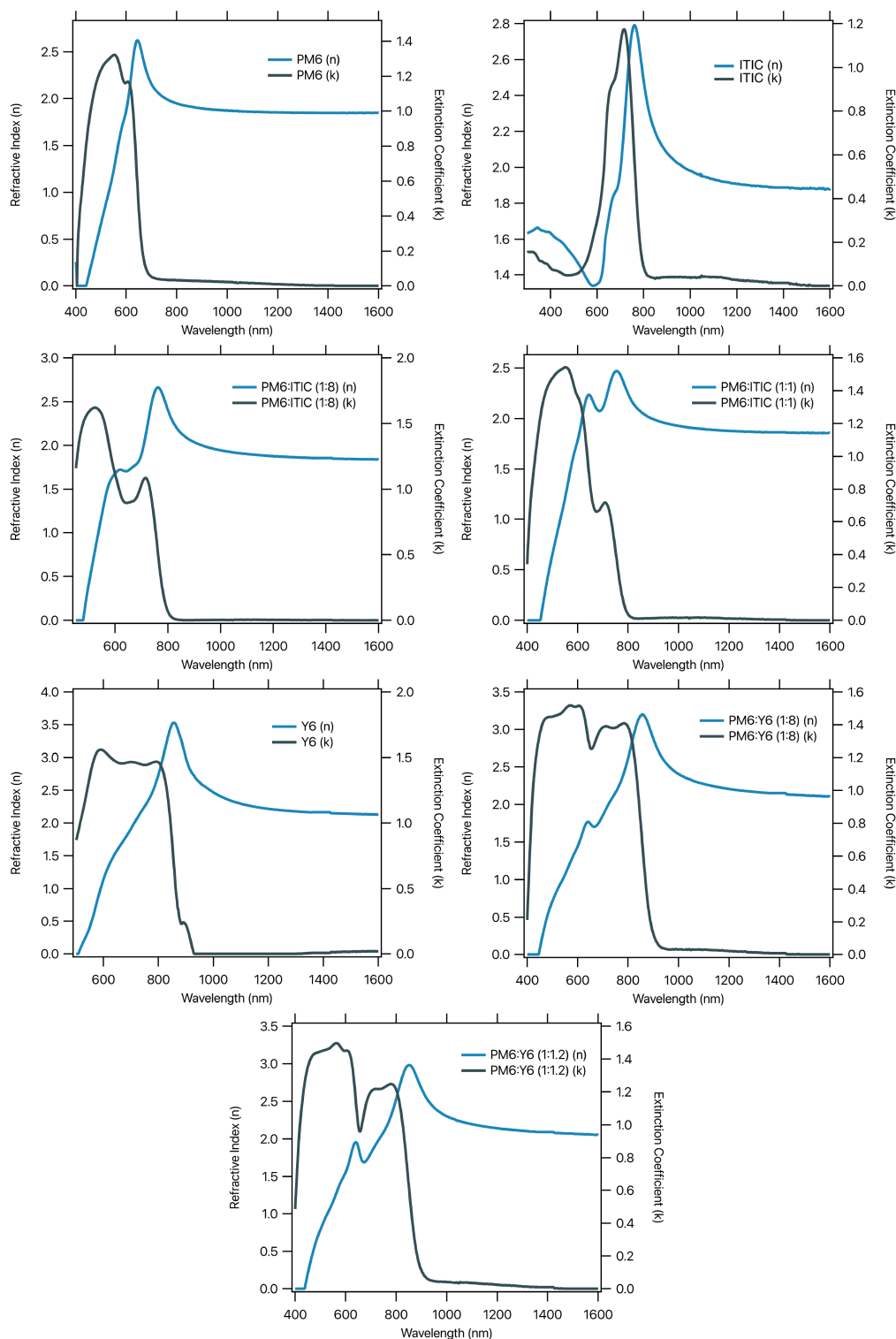
FIGURE 5.8: The refractive indices and extinction coefficients modelled for the donor and acceptor neat films and the blends of these materials. Towards the long-wavelength limit of these modelled systems, deviations from the constant refractive index occur as a result of the Cauchy approximation unsuccessfully fitting the polarisation data.

device performance for the 1:1 and 1:8 weight ratio blends was quite similar overall and so this marginal change in dielectric constant is not expected to induce a significant change in the rate of exciton dissociation. As for the ITIC-2F-based blends, it was noted that there was little difference in the dielectric constant with increasing quantities of PM6.

5.3 Active layer morphology analysis

5.3.1 Active layer surface profiles

While the application of AFM to analyse the morphology of active layer films may be limited in the sense that it is not possible to analyse the bulk structure in a similar manner to XRR and *Grazing-Incidence Wide-Angle X-ray Scattering* (GIWAXS), this method does provide some insight to the potential packing characteristics of the donor and acceptor material. The AFM images presented in Figure 5.9 show different surface roughnesses in the blend films with different donor polymer content. As shown in Table 5.8, when polymer donor content is reduced, surface roughness increases. *root mean square* (RMS) surface roughness increases from 1.24 nm (PM6:Y6 1:1 by weight) to 1.27 nm (PM6:Y6 1:8 by weight) and 1.74 nm for the neat Y6 film.

For all three film types, the RMS surface roughness of less than 2 nm was an indication of how well these advanced donor and acceptor materials can pack in the bulk. Very low surface roughness is critical in the formation of Ohmic contact between the active layer and charge transport layers so as to minimise the probability of charge recombination at these interfaces. The probability of surface defects increases exponentially with the area of the device.[43] Maintaining the low surface roughness of the 1:1 blend film when the polymer content is significantly reduced in the 1:8 blend is a promising indication that low donor content devices can maintain the good interfacial properties of optimised 1:1 blend PM6:Y6 active layer films.

Table 5.8: PM6:Y6 Film Surface Roughness

W. Ratio	RMS Roughness	Absolute Roughness
w/w	R_q (nm)	R_a (nm)
Neat Y6	1.74	1.35
1:1	1.24	0.87
1:8	1.27	0.96

Y6 Neat Film
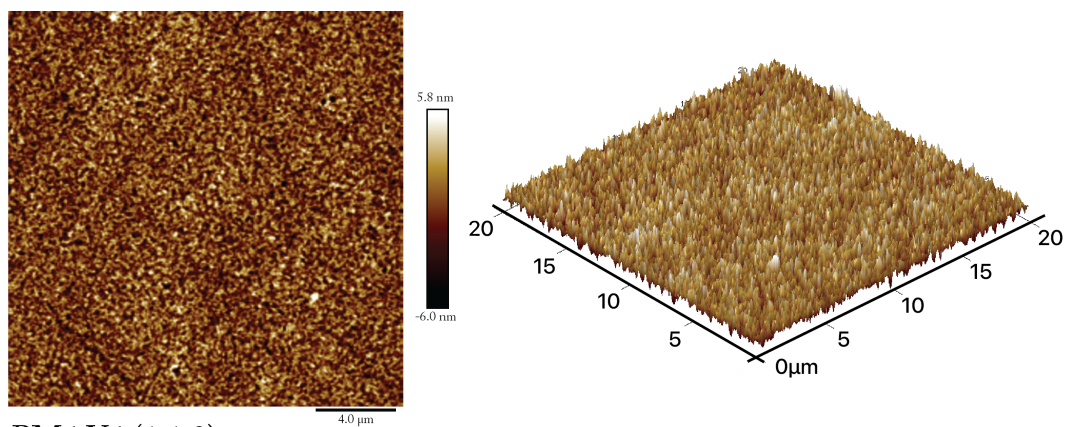
PM6:Y6 (1:1.2)
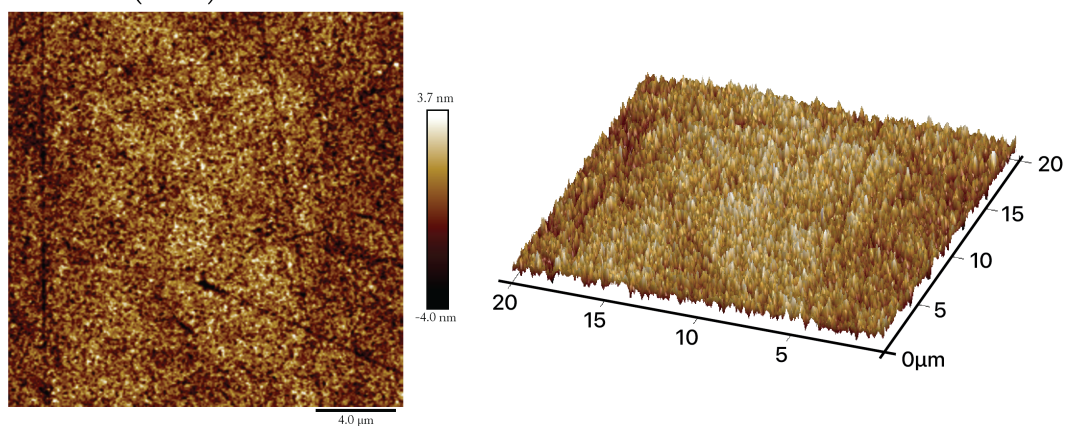
PM6:Y6 (1:8)
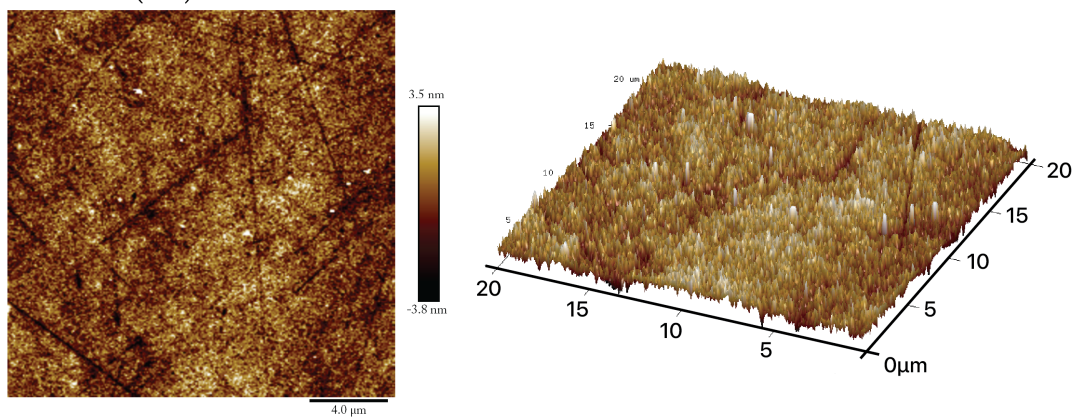
FIGURE 5.9: AFM scans performed on Y6 neat and blend films that have been prepared on ITO sputter-coated substrates with the PEDOT:PSS hole transport layer.

5.3.2 Bulk Morphology Analysis

GIWAXS and XRR were used to investigate the bulk molecular packing of both neat and blend films. The samples used for XRR analysis were the same as those that were prepared for ellipsometry on silicon substrates. These thinner films have comparable bulk morphology to slightly thicker films cast for complete devices and produce fewer diffraction peaks that can be used for more consistent modelling.

Regions of *out of plane* (OOP) stacking indicate that neat Y6 is forming locally ordered aggregations similar to the profile perspective in Figure 5.10(a). The neat Y6 film shows a strong π-π stacking peak in the OOP orientation at $q \approx 1.7$ Å^{-1}, as indicated in Figure 5.11. Using the relation,

$$d = \frac{2\pi}{q}, \tag{5.1}$$

to convert from the reciprocal space peak position to the real space molecular separation, it was determined that the packing separation between Y6 molecules in the neat film was approximately 3.7 Å. The diffraction peaks closer to the origin indicates a degree of OOP and in-plane stacking at $q \approx 0.35$ Å^{-1} with a molecular separation of 22.1 Å. This diffraction peak is typically assigned to lamellar stacking which is the weaker interaction involving the side-chains of Y6. Recent studies have indicated that these diffraction peaks may also be the result of chromophoric core ordering with the end groups of these fused-ring acceptor materials undergoing π-π stacking.[93] As for the neat PM6 film, there is a far weaker π-π peak in the OOP direction at $q \approx 1.6$ Å^{-1} which corresponds to a stacking distance of 3.9 Å with a dominant lamellar peak in the OOP direction at $q \approx 0.3$ Å^{-1} corresponding to an interaction distance of 20.9 Å.

(a) (b)
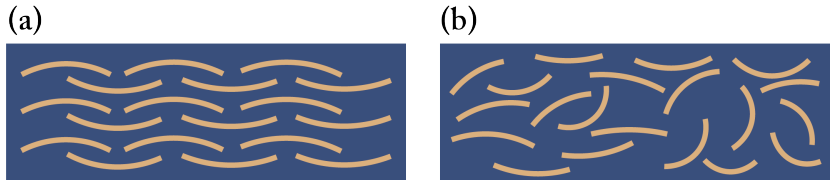
FIGURE 5.10: (a) OOP stacking indicates that the Y6 molecules are aggregating with local order as a result of their strong intermolecular π-π interactions. (b) More amorphous films, such as the neat PM6 and ITIC-2F samples, do not have strong diffraction spots on GIWAXS plots as a result of weaker local ordering.

For the PM6:Y6 blend films, it was observed that there was a strong diffraction peak for both the 1:1 and 1:8 weight ratio films in the OOP direction that can be attributed to the strong π-π stacking of Y6. In the case of the 1:1 film, this peak occurs at $q \approx 1.75$ Å^{-1} which corresponds to a packing distance of 4.0 Å. As for the in-plane direction, the diffraction pattern was quite homogenous, indicating a largely disordered system with lamellar stacking from either PM6 or Y6 with an interaction distance of 20.9 Å. The 1:8 film features a more prominent OOP stacking feature, most likely as a result of the higher weight content of Y6 in the blend. The in-plane stacking feature was slightly more prominent for the 1:8 film with a scattering peak at $q \approx 0.3$ Å^{-1}, corresponding to an interaction distance of 20.9 Å. In terms of relative film density, it is apparent from Figure 5.13 that all three films were (within measurement and modelling uncertainty) approximately equivalent. This result indicates that the change in polymer content does not greatly affect the film density characteristics. In the PM6:Y6 (1:1.2) film, however, there was an apparent increase in mass density towards the air interface. This increase does not correlate with the PM6 or Y6 scattering length densities and so it

appears that, at this blend ratio, an alternative domain arrangement that results in increased density may be forming, facilitated by the increased polymer content compared with the other films.

In the case of the ITIC-2F neat films, a far more amorphous bulk morphology was observed with the OOP scattering showing no prominent peak as was the case for Y6. This means that the donor and acceptor molecules are forming domains with a large dispersion of sizes and orientations. A lamellar peak is visible at $q \approx 0.35$ Å^{-1}, corresponding to an interaction distance of 17.9 Å. This indicates that the ITIC-2F molecules are more disordered than Y6 in the neat film with only limited long-range ordering present. It should be noted that this packing behaviour is more prevalent with most NFA small molecule materials and Y6 is quite unique in its ability to pack with a degree of order. In the blend films, a weak scattering peak was observed for the OOP orientation at $q \approx 1.6$ Å^{-1} which corresponds to a packing distance of 3.9 Å which might be attributable to the PM6 as this feature was not present in the 1:8 blend or neat films. A far more prominent features in both the 1:1 and 1:8 blend films was the presence of a high-intensity scattering peak at $q \approx 0.3$ Å^{-1}, corresponding to an interaction distance of 20.9 Å. These scattering peaks indicate the lamellar packing feature of PM6 that was also observed in the case of the PM6 neat film and PM6:Y6 blends. As demonstrated in Figure 5.13, the ITIC-2F blends were, within uncertainty, equal in scattering length density form the XRR measurements. This result indicates that, as polymer content in the film is increased, the relatively amorphous packing characteristic of ITIC-2F is not altered significantly.

Comparing the two NFAs, the *scattering length density* (SLD) from XRR of both Y6- and ITIC-2F-based films are very similar. However, when analysing the results from GIWAXS, it becomes evident that the Y6- and ITIC-2F-based films pack in very different manners, independent of the donor-acceptor blend ratio. The bulk ordering features of neat films of both PM6 and Y6 are reflected in the morphology of blend films. PM6:Y6 films demonstrate a degree of ordering that is not present in the PM6:ITIC-2F samples. Comparing these results with OPV device performance data, it becomes evident that a degree of ordering in both donor and acceptor phases leads to enhanced overall performance. As discussed in Section 5.2.1, both NFAs exhibited very similar light absorption characteristics, meaning that the difference in device performance between these acceptor materials is not a result of their ability to generate excitons. Differences in the packing characteristics of these NFAs and their blends is evident and so exciton dissociation and subsequent free charge transport may be hindered by the more amorphous structure of PM6:ITIC-2F active layers, leading to the observed lower device performance compared with Y6-based devices.
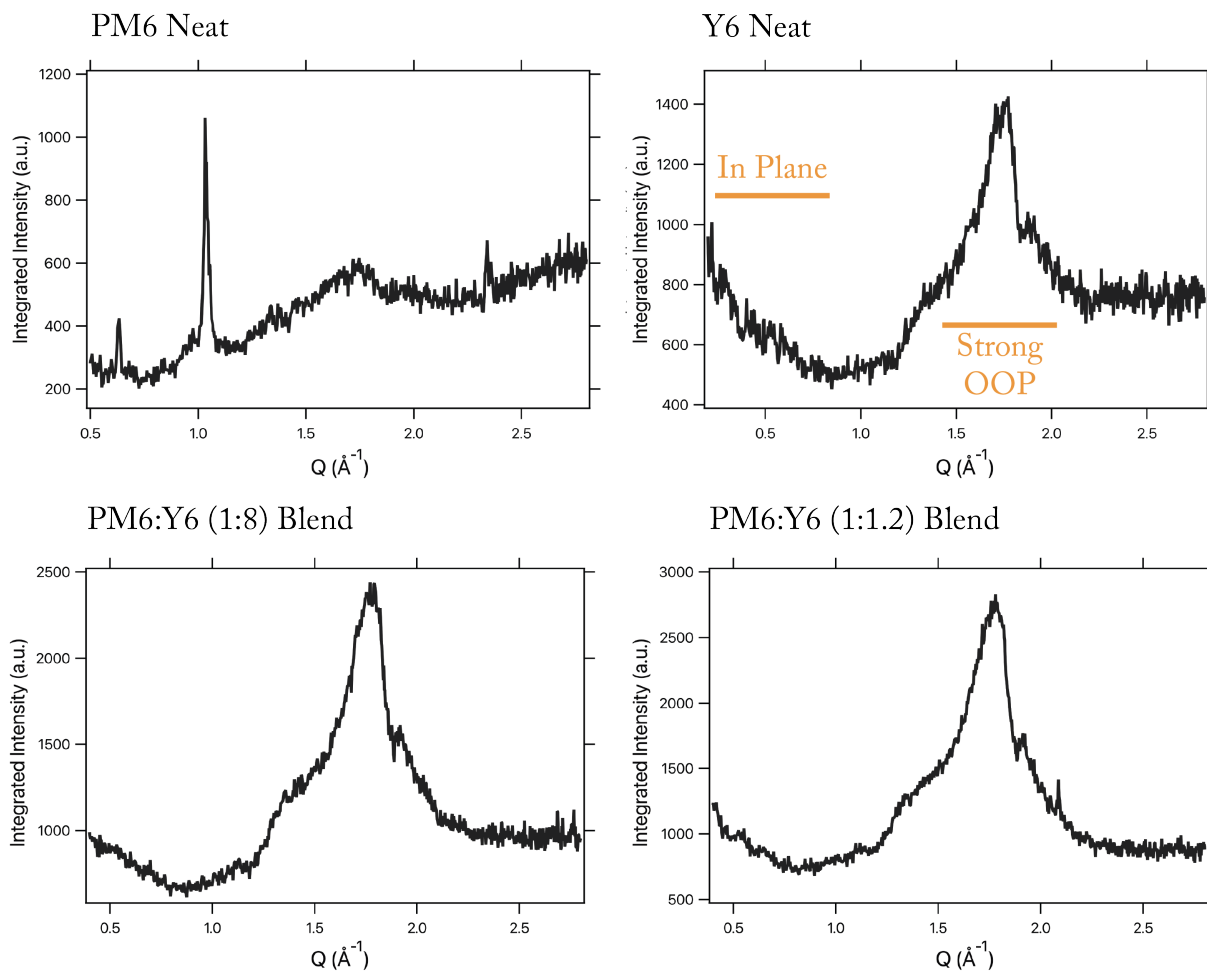
FIGURE 5.11: Integrated GIWAXS intensity plots of neat and blend films produced using PM6 and Y6. The lower panel depicts XRR scattering length density measurements for the same set of films. These measurements indicate that Y6 exhibits regions of π-π stacking and significant local ordering. Regions where in-plane and OOP stacking are visible on each of the plots are indicated.
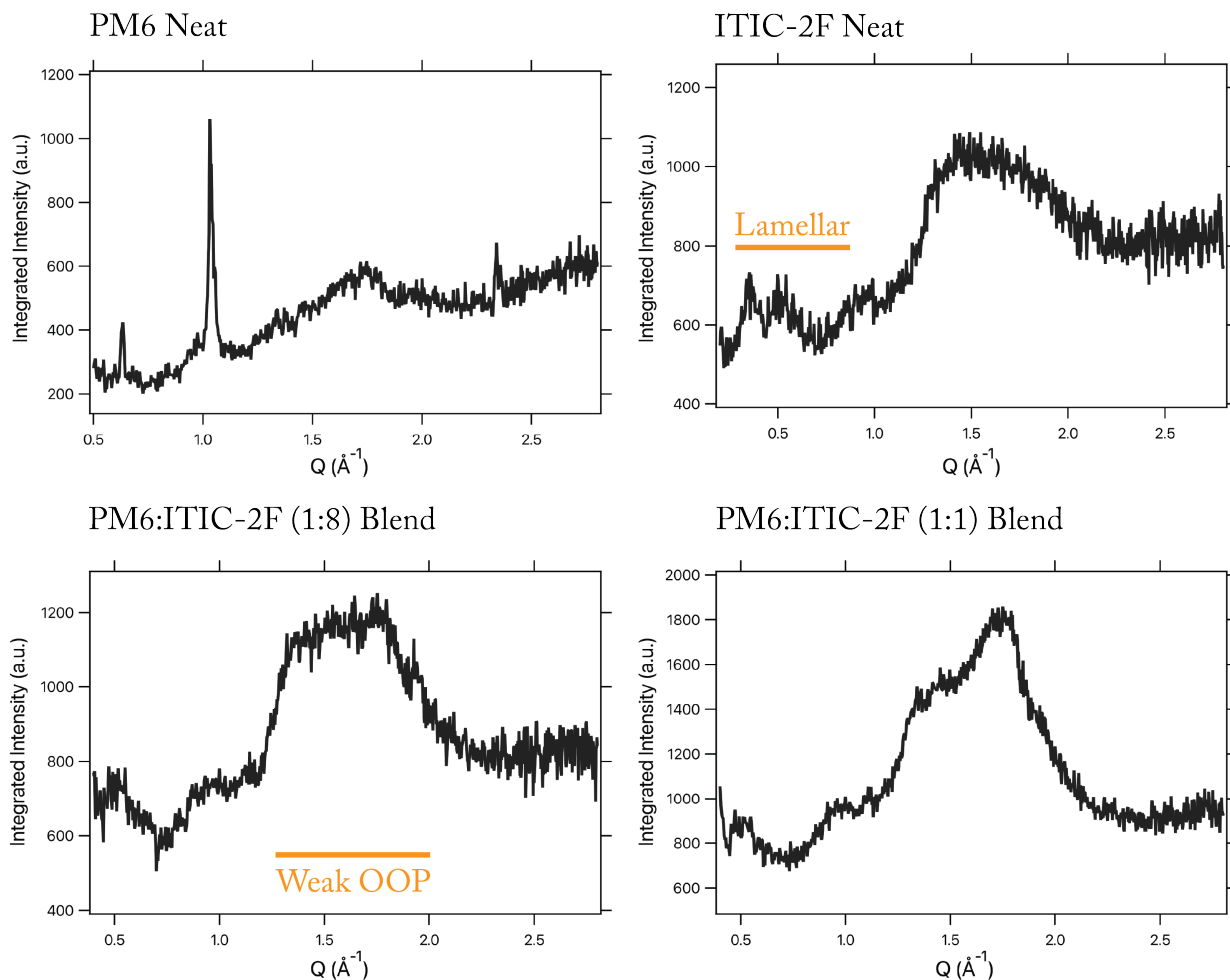
FIGURE 5.12: Integrated GIWAXS intensity plots of neat and blend films produced using PM6 and ITIC-2F. Compared with Y6, ITIC-2F presents a limited degree of local ordering, with PM6 providing the dominant lamellar features. Regions where lamellar and OOP stacking are visible on each of the plots are indicated.
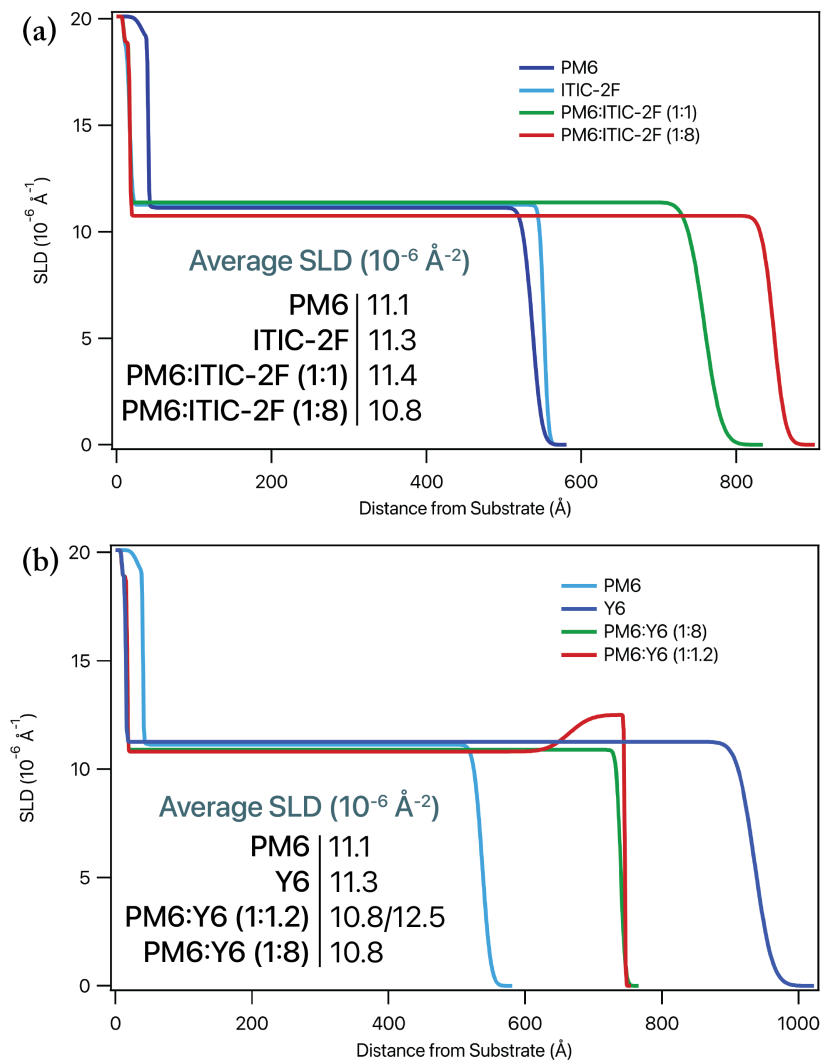
Figure 5.13: SLD measurements for (a) ITIC-based films and blends and (b) Y6-based films and blends. While the density is (within uncertainty margins) approximately equivalent for all blend ratios for both Y6- and ITIC-2F-based films, there is an increase in density for the PM6:Y6 (1:1.2) film towards the air interface. Scattering length densities for the film bulk are inset.

Conclusion & Outlook   6

This research programme aimed to investigate the performance of OPV devices using high-performance NFA materials blended with a polymeric donor at varying weight ratios. It was demonstrated that it is possible to reduce the weight content of the donor material and retain strong photovoltaic performance. Investigation of the optical and morphological properties of both the optimised and low donor content blends provided insights into the reasons behind the good photovoltaic performance of both blend ratios. Along with comparable device performance, the light absorption and morphological characteristics of blends containing a given NFA were very similar for both optimised and low donor weight ratios. Moreover, comparing the optical and morphological properties of films fabricated with each NFA material demonstrated that, independent of blend weight ratio, differences in OPV device performance for Y6 compared with ITIC-2F arose as a result of the different packing characteristics of each acceptor. It was identified that blends of PM6:Y6 produced more ordered BHJs when compared with blends of PM6:ITIC-2F, which is associated with the better OPV device performance of the former.

This research programme builds upon previous investigations into low donor content OPV devices by demonstrating that two high-performance NFA materials with very different structural and morphological packing characteristics can retain strong photovoltaic performance with reduced donor content. By demonstrating that devices fabricated using NFA materials are less sensitive to changes in blend ratio and film morphology than previously thought, this project lends weight to the further investigation into low donor content OPV device performance using high-performance organic semiconducting materials. As the selected semiconducting materials are currently being used in the fabrication of some of the best performing large-scale test devices, demonstrating that it is possible to simplify the fabrication of small-scale test devices may lead to improvements in the scalability of OPV devices with more consistent performance. Developing pathways toward commercialisation for OPV devices are essential if this technology is to contribute to the renewable energy mix.

While these initial results for low donor content device performance and characterisation are an exciting indication of potential pathways towards simplified and scalable OPV devices, further research is required to develop a truly complete understanding of the physical and optoelectronic characteristics of these devices. Now that it has been demonstrated that devices using the low-donor content blend ratio perform well when compared with "optimised" blend ratio, it would be useful to understand where the boundaries of this performance are with respect to the donor weight content in the active layer blend. Fabricating devices with a range of active layer blend weight ratios for both acceptor

materials would provide an indication of whether a point exists where device performance begins to drop significantly.

Characterising the charge transport properties of this active layer blend ratio with *metal–insulator–semiconductor charge extraction with linearly increasing voltage* (MIS-CELIV) would provide useful insight into whether a marked change in photovoltaic performance is the result of a change in the charge transport efficiency due to the decreased donor content. A comparison of charge transport rates for Y6- and ITIC-2F-based devices would also provide insight into whether the differences in OPV device performance stem from lower charge extraction efficiency for the latter NFA. Further study into the active layer morphology, particularly through the characterisation of a greater range of blend ratios, could provide insight into why certain changes in morphology still allow for good exciton diffusion and charge extraction when the donor-acceptor interfacial area is significantly reduced. Finally, further investigation into the optical properties of the materials and resultant blend films would provide a stronger justification for the differences in device performance characteristics observed in this work. In particular, an advanced application of ellipsometry to study thin-film bulk morphology could provide complementary insights to the analysis performed using X-ray techniques.

Future work based on the initial investigation presented in this thesis could extend beyond an improvement of the methods applied and depth of results. Initiating a process of scaling-up the device active area and optimising performance at each step while minimising the donor content would be an interesting way to directly test the hypothesis presented for enhanced device consistency across large areas. To fabricate larger-scale OPV devices, different solution processing techniques will be required, as will a process of iteration to develop an optimised fabrication process. Another avenue for further investigation based on the initial work of this project could focus on a more systematic study of how certain structural characteristics of the most advanced NFA materials might facilitate the strong performance we are observing for low donor content devices. Thus, this research programme has provided the groundwork for subsequent investigation that could enhance our understanding of how the fabrication of OPV devices can be simplified while retaining strong performance.

Bibliography

[1] Hannah Ritchie and Max Roser. Emissions by sector, 2020. URL https://ourworldindata.org/emissions-by-sector#energy-electricity-heat-and-transport-73-2.

[2] Hannah Ritchie and Max Roser. Renewable energy. *Our World in Data*, 2020. https://ourworldindata.org/renewable-energy.

[3] Marco Raugei, Sgouris Sgouridis, David Murphy, Vasilis Fthenakis, Rolf Frischknecht, Christian Breyer, Ugo Bardi, Charles Barnhart, Alastair Buckley, Michael Carbajales-Dale, Denes Csala, Mariska de Wild-Scholten, Garvin Heath, Arnulf Jæger-Waldau, Christopher Jones, Arthur Keller, Enrica Leccisi, Pierluigi Mancarella, Nicola Pearsall, Adam Siegel, Wim Sinke, and Philippe Stolz. Energy return on energy invested (eroei) for photovoltaic solar systems in regions of moderate insolation: A comprehensive response. *Energy Policy*, 102:377–384, 2017. ISSN 0301-4215. doi: https://doi.org/10.1016/j.enpol.2016.12.042. URL https://www.sciencedirect.com/science/article/pii/S0301421516307066.

[4] Nieves Espinosa, Markus Hösel, Dechan Angmo, and Frederik C. Krebs. Solar cells with one-day energy payback for the factories of the future. *Energy Environ. Sci.*, 5:5117–5132, 2012. doi: 10.1039/C1EE02728J. URL http://dx.doi.org/10.1039/C1EE02728J.

[5] Subhes C. Bhattacharyya and Debajit Palit. Mini-grid based off-grid electrification to enhance electricity access in developing countries: What policies may be required? *Energy Policy*, 94: 166–178, 2016. ISSN 0301-4215. doi: https://doi.org/10.1016/j.enpol.2016.04.010. URL https://www.sciencedirect.com/science/article/pii/S0301421516301781.

[6] Daniela Sica, Ornella Malandrino, Stefania Supino, Mario Testa, and Maria Lucchetti. Management of end-of-life photovoltaic panels as a step towards a circular economy. *Renewable and Sustainable Energy Reviews*, 82, 11 2017. doi: 10.1016/j.rser.2017.10.039.

[7] Hugo Bronstein, Christian B. Nielsen, Bob C. Schroeder, and Iain McCulloch. The role of chemical design in the performance of organic semiconductors. *Nature Reviews Chemistry*, 4(2):66–77, 2020. doi: 10.1038/s41570-019-0152-9. URL https://doi.org/10.1038/s41570-019-0152-9.

[8] Guangye Zhang, Jingbo Zhao, Philip C. Y. Chow, Kui Jiang, Jianquan Zhang, Zonglong Zhu, Jie Zhang, Fei Huang, and He Yan. Nonfullerene acceptor molecules for bulk heterojunction organic solar cells. *Chemical Reviews*, 118(7):3447–3507, 2018. doi: 10.1021/acs.chemrev.7b00535. URL https://doi.org/10.1021/acs.chemrev.7b00535. PMID: 29557657.

[9] Ardalan Armin, Wei Li, Oskar J. Sandberg, Zuo Xiao, Liming Ding, Jenny Nelson, Dieter Neher, Koen Vandewal, Safa Shoaee, Tao Wang, Harald Ade, Thomas Heumüller, Christoph

Brabec, and Paul Meredith. A history and perspective of non-fullerene electron acceptors for organic solar cells. *Advanced Energy Materials*, 11(15):2003570, 2021. doi: https://doi.org/10.1002/aenm.202003570. URL https://onlinelibrary.wiley.com/doi/abs/10.1002/aenm.202003570.

[10] Justin M. Hodgkiss. No free lunch for non-fullerene acceptors. *Nature Materials*, 20 (3):289–290, 2021. doi: 10.1038/s41563-020-00836-w. URL https://doi.org/10.1038/s41563-020-00836-w.

[11] Bert Männg, Martin Pfeiffer, and Christian Uhrich. Photoactive device with organic layers, April 2010.

[12] Vincenzo Pecunia, Luigi G. Occhipinti, and Robert L. Z. Hoye. Emerging indoor photovoltaic technologies for sustainable internet of things. *Advanced Energy Materials*, n/a(n/a):2100698. doi: https://doi.org/10.1002/aenm.202100698. URL https://onlinelibrary.wiley.com/doi/abs/10.1002/aenm.202100698.

[13] Marie Jakešová, Theresia Arbring Sjöström, Vedran Đerek, David Poxson, Magnus Berggren, Eric Daniel Głowacki, and Daniel T. Simon. Wireless organic electronic ion pumps driven by photovoltaics. *npj Flexible Electronics*, 3(1):14, 2019. doi: 10.1038/s41528-019-0060-6. URL https://doi.org/10.1038/s41528-019-0060-6.

[14] Osbel Almora, Derya Baran, Guillermo C. Bazan, Christian Berger, Carlos I. Cabrera, Kylie R. Catchpole, Sule Erten-Ela, Fei Guo, Jens Hauch, Anita W. Y. Ho-Baillie, T. Jesper Jacobsson, Rene A. J. Janssen, Thomas Kirchartz, Nikos Kopidakis, Yongfang Li, Maria A. Loi, Richard R. Lunt, Xavier Mathew, Michael D. McGehee, Jie Min, David B. Mitzi, Mohammad K. Nazeeruddin, Jenny Nelson, Ana F. Nogueira, Ulrich W. Paetzold, Nam-Gyu Park, Barry P. Rand, Uwe Rau, Henry J. Snaith, Eva Unger, Lídice Vaillant-Roca, Hin-Lap Yip, and Christoph J. Brabec. Device performance of emerging photovoltaic materials (version 1). *Advanced Energy Materials*, 11(11):2002774, 2021. doi: https://doi.org/10.1002/aenm.202002774. URL https://onlinelibrary.wiley.com/doi/abs/10.1002/aenm.202002774.

[15] Sunsun Li, Long Ye, Wenchao Zhao, Shaoqing Zhang, Subhrangsu Mukherjee, Harald Ade, and Jianhui Hou. Energy-level modulation of small-molecule electron acceptors to achieve over 12% efficiency in polymer solar cells. *Advanced Materials*, 28(42):9423–9429, 2016. doi: https://doi.org/10.1002/adma.201602776. URL https://onlinelibrary.wiley.com/doi/abs/10.1002/adma.201602776.

[16] Hongzhen Lin and Fenglian Bai. *Electronic Process in Organic Solids*, chapter 1, pages 1–42. Wiley, 2013. ISBN 9783527653454. doi: https://doi.org/10.1002/9783527653454.ch1. URL https://onlinelibrary.wiley.com/doi/abs/10.1002/9783527653454.ch1.

[17] Wolfgang Tress. *Organic Solar Cells*, volume 208. Springer, 1 edition, 2014.

[18] Jean-Luc Bredas. Mind the gap! *Mater. Horiz.*, 1:17–19, 2014. doi: 10.1039/C3MH00098B. URL http://dx.doi.org/10.1039/C3MH00098B.

[19] Hongzhen Lin and Fenglian Bai. *Organic Optoelectronics*, chapter 1. Wiley, 2013.

[20] Zhenzhen Zhang, Jun Yuan, Qingya Wei, and Yingping Zou. Small-molecule electron acceptors for efficient non-fullerene organic solar cells. *Frontiers in Chemistry*, 6:414, 2018. ISSN

2296-2646. doi: 10.3389/fchem.2018.00414. URL https://www.frontiersin.org/article/10.3389/fchem.2018.00414.

[21] Tanya Kumari, Sang Myeon Lee, So-Huei Kang, Shanshan Chen, and Changduk Yang. Ternary solar cells with a mixed face-on and edge-on orientation enable an unprecedented efficiency of 12.1 *Energy Environ. Sci.*, 10:258–265, 2017. doi: 10.1039/C6EE02851A. URL http://dx.doi.org/10.1039/C6EE02851A.

[22] Itaru Osaka. Semiconducting polymers based on electron-deficient π-building units. *Polymer Journal*, 47(1):18–25, 2015. doi: 10.1038/pj.2014.90. URL https://doi.org/10.1038/pj.2014.90.

[23] N. S. Sariciftci, L. Smilowitz, A. J. Heeger, and F. Wudl. Photoinduced electron transfer from a conducting polymer to buckminsterfullerene. *Science*, 258(5087):1474–1476, 1992. ISSN 0036-8075. doi: 10.1126/science.258.5087.1474. URL https://science.sciencemag.org/content/258/5087/1474.

[24] J. Koskinen. 4.02 - cathodic-arc and thermal-evaporation deposition. In Saleem Hashmi, Gilmar Ferreira Batalha, Chester J. Van Tyne, and Bekir Yilbas, editors, *Comprehensive Materials Processing*, pages 3–55. Elsevier, Oxford, 2014. ISBN 978-0-08-096533-8. doi: https://doi.org/10.1016/B978-0-08-096532-1.00409-X. URL https://www.sciencedirect.com/science/article/pii/B978008096532100409X.

[25] Liang Shi, Chee Kong Lee, and Adam P. Willard. The enhancement of interfacial exciton dissociation by energetic disorder is a nonequilibrium effect. *ACS Central Science*, 3(12):1262–1270, 12 2017. doi: 10.1021/acscentsci.7b00404. URL https://doi.org/10.1021/acscentsci.7b00404.

[26] Andrius Devižis, Jelissa De Jonghe-Risse, Roland Hany, Frank Nüesch, Sandra Jenatsch, Vidmantas Gulbinas, and Jacques-E. Moser. Dissociation of charge transfer states and carrier separation in bilayer organic solar cells: A time-resolved electroabsorption spectroscopy study. *Journal of the American Chemical Society*, 137(25):8192–8198, 07 2015. doi: 10.1021/jacs.5b03682. URL https://doi.org/10.1021/jacs.5b03682.

[27] David Kearns and Melvin Calvin. Photovoltaic effect and photoconductivity in laminated organic systems. *The Journal of Chemical Physics*, 29(4):950–951, 1958. doi: 10.1063/1.1744619. URL https://doi.org/10.1063/1.1744619.

[28] C. W. Tang. Two-layer organic photovoltaic cell. *Applied Physics Letters*, 48(2):183–185, 1986. doi: 10.1063/1.96937. URL https://doi.org/10.1063/1.96937.

[29] Masahiro Hiramoto and Yusuke Shinmura. *Organic Solar Cells*, pages 1–1. Springer International Publishing, Cham, 2017. ISBN 978-3-319-48933-9. doi: 10.1007/978-3-319-48933-9_54. URL https://doi.org/10.1007/978-3-319-48933-9_54.

[30] Hansol Lee, Chaneui Park, Dong Hun Sin, Jong Hwan Park, and Kilwon Cho. Recent advances in morphology optimization for organic photovoltaics. *Advanced Materials*, 30(34):1800453, 2018. doi: https://doi.org/10.1002/adma.201800453. URL https://onlinelibrary.wiley.com/doi/abs/10.1002/adma.201800453.

[31] Benjamin Y. Finck and Benjamin J. Schwartz. Drift-diffusion studies of compositional morphology in bulk heterojunctions: The role of the mixed phase in photovoltaic performance. *Phys. Rev. Applied*, 6:054008, Nov 2016. doi: 10.1103/PhysRevApplied.6.054008. URL https://link.aps.org/doi/10.1103/PhysRevApplied.6.054008.

[32] Mariano Campoy-Quiles, Toby Ferenczi, Tiziano Agostinelli, Pablo G. Etchegoin, Youngkyoo Kim, Thomas D. Anthopoulos, Paul N. Stavrinou, Donal D. C. Bradley, and Jenny Nelson. Morphology evolution via self-organization and lateral and vertical diffusion in polymer:fullerene solar cell blends. *Nature Materials*, 7(2):158–164, 2008. doi: 10.1038/nmat2102. URL https://doi.org/10.1038/nmat2102.

[33] Dani M. Stoltzfus, Jenny E. Donaghey, Ardalan Armin, Paul E. Shaw, Paul L. Burn, and Paul Meredith. Charge generation pathways in organic solar cells: Assessing the contribution from the electron acceptor. *Chemical Reviews*, 116(21):12920–12955, 2016. doi: 10.1021/acs.chemrev.6b00126. URL https://doi.org/10.1021/acs.chemrev.6b00126. PMID: 27341081.

[34] Pei Cheng, Gang Li, Xiaowei Zhan, and Yang Yang. Next-generation organic photovoltaics based on non-fullerene acceptors. *Nature Photonics*, 12(3):131–142, 2018. doi: 10.1038/s41566-018-0104-9. URL https://doi.org/10.1038/s41566-018-0104-9.

[35] Karl Leo. *Elementary Processes in Organic Photovoltaics*, volume 272. 01 2017. ISBN 978-3-319-28336-4. doi: 10.1007/978-3-319-28338-8.

[36] Ishan C. Ghosekar and Ganesh C. Patil. Impact of concentration variation and thermal annealing on performance of multilayer osc consisting of sandwiched p3ht layer between pedot:pss and p3ht:pcbm. *Microelectronic Engineering*, 221:111195, 2020. ISSN 0167-9317. doi: https://doi.org/10.1016/j.mee.2019.111195. URL https://www.sciencedirect.com/science/article/pii/S016793171930351X.

[37] Sayantan Das and T. L. Alford. Optimization of the zinc oxide electron transport layer in p3ht:pc61bm based organic solar cells by annealing and yttrium doping. *RSC Adv.*, 5:45586–45591, 2015. doi: 10.1039/C5RA05258K. URL http://dx.doi.org/10.1039/C5RA05258K.

[38] Yanming Sun, Jung Hwa Seo, Christopher J. Takacs, Jason Seifter, and Alan J. Heeger. Inverted polymer solar cells integrated with a low-temperature-annealed sol-gel-derived zno film as an electron transport layer. *Advanced Materials*, 23(14):1679–1683, 2011. doi: https://doi.org/10.1002/adma.201004301. URL https://onlinelibrary.wiley.com/doi/abs/10.1002/adma.201004301.

[39] Yuhang Liu, Cheng Mu, Kui Jiang, Jingbo Zhao, Yunke Li, Lu Zhang, Zhengke Li, Joshua Yuk Lin Lai, Huawei Hu, Tingxuan Ma, Rongrong Hu, Demei Yu, Xuhui Huang, Ben Zhong Tang, and He Yan. A tetraphenylethylene core-based 3d structure small molecular acceptor enabling efficient non-fullerene organic solar cells. *Advanced Materials*, 27(6):1015–1020, 2015. doi: https://doi.org/10.1002/adma.201404152. URL https://onlinelibrary.wiley.com/doi/abs/10.1002/adma.201404152.

[40] Xinchen Li, Fengxian Xie, Shaoqing Zhang, Jianhui Hou, and Wallace CH Choy. Moox and v2ox as hole and electron transport layers through functionalized intercalation in normal and inverted organic optoelectronic devices. *Light: Science & Applications*, 4(4):e273–e273, 2015. doi: 10.1038/lsa.2015.46. URL https://doi.org/10.1038/lsa.2015.46.

[41] Wei Jiang, Chen Tao, Martin Stolterfoht, Hui Jin, Meera Stephen, Qianqian Lin, Ravi C.R. Nagiri, Paul L. Burn, and Ian R. Gentle. Hole-transporting materials for low donor content organic solar cells: Charge transport and device performance. *Organic Electronics*, 76:105480, 2020. ISSN 1566-1199. doi: https://doi.org/10.1016/j.orgel.2019.105480. URL https://www.sciencedirect.com/science/article/pii/S1566119919305075.

[42] Thomas Lee, Audrey Sanzogni, Ningxin Zhangzhou, Paul L. Burn, and Alan E. Mark. Morphology of a bulk heterojunction photovoltaic cell with low donor concentration. *ACS Applied Materials & Interfaces*, 10(38):32413–32419, 2018. doi: 10.1021/acsami.8b10321. URL https://doi.org/10.1021/acsami.8b10321. PMID: 30152227.

[43] Fei Qin, Lulu Sun, Hongting Chen, Yang Liu, Xin Lu, Wen Wang, Tiefeng Liu, Xinyun Dong, Pei Jiang, Youyu Jiang, Lei Wang, and Yinhua Zhou. 54 cm2 large-area flexible organic solar modules with efficiency above 13%. *Advanced Materials*, 33(39):2103017, 2021. doi: https://doi.org/10.1002/adma.202103017. URL https://onlinelibrary.wiley.com/doi/abs/10.1002/adma.202103017.

[44] Leiping Duan, Naveen Kumar Elumalai, Yu Zhang, and Ashraf Uddin. Progress in non-fullerene acceptor based organic solar cells. *Solar Energy Materials and Solar Cells*, 193:22–65, 2019. ISSN 0927-0248. doi: https://doi.org/10.1016/j.solmat.2018.12.033. URL https://www.sciencedirect.com/science/article/pii/S0927024818306111.

[45] Wenchao Zhao, Sunsun Li, Huifeng Yao, Shaoqing Zhang, Yun Zhang, Bei Yang, and Jianhui Hou. Molecular optimization enables over 13% efficiency in organic solar cells. *Journal of the American Chemical Society*, 139(21):7148–7151, 2017. doi: 10.1021/jacs.7b02677. URL https://doi.org/10.1021/jacs.7b02677. PMID: 28513158.

[46] Ji Xiong, Jingui Xu, Yufan Jiang, Zuo Xiao, Qinye Bao, Feng Hao, Yaqing Feng, Bin Zhang, Zhiwen Jin, and Liming Ding. Fused-ring bislactone building blocks for polymer donors. *Science Bulletin*, 65, 07 2020. doi: 10.1016/j.scib.2020.07.018.

[47] Thomas Kirchartz, Kurt Taretto, and Uwe Rau. Efficiency limits of organic bulk heterojunction solar cells. *The Journal of Physical Chemistry C*, 113(41):17958–17966, 10 2009. doi: 10.1021/jp906292h. URL https://doi.org/10.1021/jp906292h.

[48] Fuwen Zhao, Huotian Zhang, Rui Zhang, Jun Yuan, Dan He, Yingping Zou, and Feng Gao. Emerging approaches in enhancing the efficiency and stability in non-fullerene organic solar cells. *Advanced Energy Materials*, 10(47):2002746, 2020. doi: https://doi.org/10.1002/aenm.202002746. URL https://onlinelibrary.wiley.com/doi/abs/10.1002/aenm.202002746.

[49] Lorena Perdigón-Toro, Huotian Zhang, Anastasia Markina, Jun Yuan, Seyed Mehrdad Hosseini, Christian M. Wolff, Guangzheng Zuo, Martin Stolterfoht, Yingping Zou, Feng Gao, Denis Andrienko, Safa Shoaee, and Dieter Neher. Barrierless free charge generation in the high-performance pm6:y6 bulk heterojunction non-fullerene solar cell. *Advanced Materials*, 32 (9):1906763, 2020. doi: https://doi.org/10.1002/adma.201906763. URL https://onlinelibrary.wiley.com/doi/abs/10.1002/adma.201906763.

[50] Leiping Duan, Yu Zhang, Haimang Yi, Faiazul Haque, Rong Deng, Huilan Guan, Yingping Zou, and Ashraf Uddin. Trade-off between exciton dissociation and carrier recombination and dielectric properties in y6-sensitized nonfullerene ternary organic solar cells. *Energy Technology*, 8(1):1900924, 2020. doi: https://doi.org/10.1002/ente.201900924. URL https://onlinelibrary.wiley.com/doi/abs/10.1002/ente.201900924.

[51] Guanran Zhang, Alex S. Loch, Mohammad Babazadeh, Paul L. Burn, and Paul E. Shaw. Determining the correlation between excited state dynamics and donor and acceptor structure in nonfullerene acceptors. *The Journal of Physical Chemistry C*, 124(33):17851–17863, 2020. doi: 10.1021/acs.jpcc.0c01402. URL https://doi.org/10.1021/acs.jpcc.0c01402.

[52] Yuze Lin, Jiayu Wang, Zhi-Guo Zhang, Huitao Bai, Yongfang Li, Daoben Zhu, and Xiaowei Zhan. An electron acceptor challenging fullerenes for efficient polymer solar cells. *Advanced Materials*, 27(7):1170–1174, 2015. doi: https://doi.org/10.1002/adma.201404317. URL https://onlinelibrary.wiley.com/doi/abs/10.1002/adma.201404317.

[53] Yankang Yang, Zhi-Guo Zhang, Haijun Bin, Shanshan Chen, Liang Gao, Lingwei Xue, Changduk Yang, and Yongfang Li. Side-chain isomerization on an n-type organic semiconductor itic acceptor makes 11.77% high efficiency polymer solar cells. *Journal of the American Chemical Society*, 138(45):15011–15018, 11 2016. doi: 10.1021/jacs.6b09110. URL https://doi.org/10.1021/jacs.6b09110.

[54] Long Ye, Wenchao Zhao, Sunsun Li, Subhrangsu Mukherjee, Joshua H. Carpenter, Omar Awartani, Xuechen Jiao, Jianhui Hou, and Harald Ade. High-efficiency nonfullerene organic solar cells: Critical factors that affect complex multi-length scale morphology and device performance. *Advanced Energy Materials*, 7(7):1602000, 2017. doi: https://doi.org/10.1002/aenm.201602000. URL https://onlinelibrary.wiley.com/doi/abs/10.1002/aenm.201602000.

[55] Huiliang Sun, Tao Liu, Jianwei Yu, Tsz-Ki Lau, Guangye Zhang, Yujie Zhang, Mengyao Su, Yumin Tang, Ruijie Ma, Bin Liu, Jiaen Liang, Kui Feng, Xinhui Lu, Xugang Guo, Feng Gao, and He Yan. A monothiophene unit incorporating both fluoro and ester substitution enabling high-performance donor polymers for non-fullerene solar cells with 16.4*Energy Environ. Sci.*, 12: 3328–3337, 2019. doi: 10.1039/C9EE01890E. URL http://dx.doi.org/10.1039/C9EE01890E.

[56] Yuliar Firdaus, Vincent M. Le Corre, Jafar I. Khan, Zhipeng Kan, Frédéric Laquai, Pierre M. Beaujuge, and Thomas D. Anthopoulos. Key parameters requirements for non-fullerene-based organic solar cells with power conversion efficiency >20%. *Advanced Science*, 6(9):1802028, 2019. doi: https://doi.org/10.1002/advs.201802028. URL https://onlinelibrary.wiley.com/doi/abs/10.1002/advs.201802028.

[57] Wenchao Zhao, Sunsun Li, Huifeng Yao, Shaoqing Zhang, Yun Zhang, Bei Yang, and Jianhui Hou. Molecular optimization enables over 13cells. *Journal of the American Chemical Society*, 139: 7148–7151, 05 2017. doi: 10.1021/jacs.7b02677.

[58] Maojie Zhang, Xia Guo, Shaoqing Zhang, and Jianhui Hou. Synergistic effect of fluorination on molecular energy level modulation in highly efficient photovoltaic polymers. *Advanced Materials*, 26(7):1118–1123, 2014. doi: https://doi.org/10.1002/adma.201304427. URL https://onlinelibrary.wiley.com/doi/abs/10.1002/adma.201304427.

[59] Kazuaki Kawashima, Tomohiro Fukuhara, Yousuke Suda, Yasuhito Suzuki, Tomoyuki Koganezawa, Hiroyuki Yoshida, Hideo Ohkita, Itaru Osaka, and Kazuo Takimiya. Implication of fluorine atom on electronic properties, ordering structures, and photovoltaic performance in naphthobisthiadiazole-based semiconducting polymers. *Journal of the American Chemical Society*, 138(32):10265–10275, 08 2016. doi: 10.1021/jacs.6b05418. URL https://doi.org/10.1021/jacs.6b05418.

[60] Katharina Reichenbächer, Heike I. Süss, and Jürg Hulliger. Fluorine in crystal engineering—"the little atom that could". *Chem. Soc. Rev.*, 34:22–30, 2005. doi: 10.1039/B406892K. URL http://dx.doi.org/10.1039/B406892K.

[61] Andrew C Stuart, John R Tumbleston, Huaxing Zhou, Wentao Li, Shubin Liu, Harald Ade, and Wei You. Fluorine substituents reduce charge recombination and drive structure and morphology

development in polymer solar cells. *J Am Chem Soc*, 135(5):1806–1815, Feb 2013. ISSN 1520-5126 (Electronic); 0002-7863 (Linking). doi: 10.1021/ja309289u.

[62] Ossila. Itic-2f (n-type acceptor), n.d.. URL https://www.ossila.com/products/itic-2f.

[63] Jun Yuan, Yunqiang Zhang, Liuyang Zhou, Guichuan Zhang, Hin-Lap Yip, Tsz-Ki Lau, Xinhui Lu, Can Zhu, Hongjian Peng, Paul A. Johnson, Mario Leclerc, Yong Cao, Jacek Ulanski, Yongfang Li, and Yingping Zou. Single-junction organic solar cell with over 15fused-ring acceptor with electron-deficient core. *Joule*, 3(4):1140–1151, 2019. ISSN 2542-4351. doi: https://doi.org/10.1016/j.joule.2019.01.004. URL https://www.sciencedirect.com/science/article/pii/S2542435119300327.

[64] Haiyan Chen, Dingqin Hu, Qianguang Yang, Jie Gao, Jiehao Fu, Ke Yang, Hao He, Shanshan Chen, Zhipeng Kan, Tainan Duan, Changduk Yang, Jianyong Ouyang, Zeyun Xiao, Kuan Sun, and Shirong Lu. All-small-molecule organic solar cells with an ordered liquid crystalline donor. *Joule*, 3(12):3034–3047, 2019. ISSN 2542-4351. doi: https://doi.org/10.1016/j.joule.2019.09.009. URL https://www.sciencedirect.com/science/article/pii/S2542435119304696.

[65] Xuelin Wang, Qianqian Sun, Jinhua Gao, Xiaoling Ma, Jae Hoon Son, Sang Young Jeong, Zhenghao Hu, Lianbin Niu, Han Young Woo, Jian Zhang, and Fujun Zhang. Ternary organic photovoltaic cells exhibiting 17.59% efficiency with two compatible y6 derivations as acceptor. *Solar RRL*, 5(3):2100007, 2021. doi: https://doi.org/10.1002/solr.202100007. URL https://onlinelibrary.wiley.com/doi/abs/10.1002/solr.202100007.

[66] Jinfeng Ge, Lingchao Xie, Ruixiang Peng, Billy Fanady, Jiaming Huang, Wei Song, Tingting Yan, Wenxia Zhang, and Ziyi Ge. 13.34 % efficiency non-fullerene all-small-molecule organic solar cells enabled by modulating the crystallinity of donors via a fluorination strategy. *Angew Chem Int Ed Engl*, 59(7):2808–2815, Feb 2020. ISSN 1521-3773 (Electronic); 1433-7851 (Linking). doi: 10.1002/anie.201910297.

[67] Yiqun Xiao, Jun Yuan, Guodong Zhou, Ka Chak Ngan, Xinxin Xia, Jingshuai Zhu, Yingping Zou, Ni Zhao, Xiaowei Zhan, and Xinhui Lu. Unveiling the crystalline packing of y6 in thin films by thermal induced "backbone-on" orientation. *J. Mater. Chem. A*, pages –, 2021. doi: 10.1039/D1TA05268C. URL http://dx.doi.org/10.1039/D1TA05268C.

[68] Guichuan Zhang, Xian-Kai Chen, Xiao Jingyang, Philip Chow, Minrun Ren, Grit Kupgan, Xuechen Jiao, Christopher Chan, Xiaoyan Du, Ruoxi Xia, Ziming Chen, Jun Yuan, Yunqiang Zhang, Shoufeng Zhang, Yidan Liu, Yingping Zou, He Yan, Kam Wong, Veaceslav Coropceanu, and Yong Cao. Delocalization of exciton and electron wavefunction in non-fullerene acceptor molecules enables efficient organic solar cells. *Nature Communications*, 11:3943, 08 2020. doi: 10.1038/s41467-020-17867-1.

[69] Ming Zhang, Lei Zhu, Tianyu Hao, Guanqing Zhou, Chaoqun Qiu, Zhe Zhao, Nicolai Hartmann, Biao Xiao, Yecheng Zou, Wei Feng, Haiming Zhu, Maojie Zhang, Yongming Zhang, Yongfang Li, Thomas P. Russell, and Feng Liu. High-efficiency organic photovoltaics using eutectic acceptor fibrils to achieve current amplification. *Advanced Materials*, 33(18):2007177, 2021. doi: https://doi.org/10.1002/adma.202007177. URL https://onlinelibrary.wiley.com/doi/abs/10.1002/adma.202007177.

[70] Yunpeng Qin, Ye Xu, Zhengxing Peng, Jianhui Hou, and Harald Ade. Low temperature aggregation transitions in n3 and y6 acceptors enable double-annealing method that yields hierarchical morphology and superior efficiency in nonfullerene organic solar cells. *Advanced Functional Materials*, 30(46):2005011, 2020. doi: https://doi.org/10.1002/adfm.202005011. URL https://onlinelibrary.wiley.com/doi/abs/10.1002/adfm.202005011.

[71] Ji Xiong, Jingui Xu, Yufan Jiang, Zuo Xiao, Qinye Bao, Feng Hao, Yaqing Feng, Bin Zhang, Zhiwen Jin, and Liming Ding. Fused-ring bislactone building blocks for polymer donors. *Science Bulletin*, 65(21):1792–1795, 2020. ISSN 2095-9273. doi: https://doi.org/10.1016/j.scib.2020.07.018. URL https://www.sciencedirect.com/science/article/pii/S2095927320304758.

[72] Ossila. Y6 (btp-4f), n.d.. URL https://www.ossila.com/products/y6.

[73] Dinesh P.R. Thanu, Mingrui Zhao, Zhenxing Han, and Manish Keswani. Chapter 1 - fundamentals and applications of sonic technology. In Rajiv Kohli and K.L. Mittal, editors, *Developments in Surface Contamination and Cleaning: Applications of Cleaning Techniques*, pages 1–48. Elsevier, 2019. ISBN 978-0-12-815577-6. doi: https://doi.org/10.1016/B978-0-12-815577-6.00001-3. URL https://www.sciencedirect.com/science/article/pii/B9780128155776000013.

[74] D. A. Bolon and C. O. Kunz. Ultraviolet depolymerization of photoresist polymers. *Polymer Engineering & Science*, 12(2):109–111, 1972. doi: https://doi.org/10.1002/pen.760120206. URL https://onlinelibrary.wiley.com/doi/abs/10.1002/pen.760120206.

[75] Moorthi Pichumani, Payam Bagheri, Kristin M. Poduska, Wenceslao González-Viñas, and Anand Yethiraj. Dynamics, crystallization and structures in colloid spin coating. *Soft Matter*, 9:3220–3229, 2013. doi: 10.1039/C3SM27455A. URL http://dx.doi.org/10.1039/C3SM27455A.

[76] Jon Griffin, Hadi Hassan, and Emma Spooner. Spin coating: Complete guide to theory and techniques, n.d. URL https://www.ossila.com/pages/spin-coating.

[77] Donald M. Mattox. Deposition processes. In Donald M. Mattox, editor, *The Foundations of Vacuum Coating Technology*, pages 11–33. William Andrew Publishing, Norwich, NY, 2003. ISBN 978-0-8155-1495-4. doi: https://doi.org/10.1016/B978-081551495-4.50009-7. URL https://www.sciencedirect.com/science/article/pii/B9780815514954500097.

[78] NREL. Reference air mass 1.5 spectra, n.d. URL https://www.nrel.gov/grid/solar-resource/spectra-am1.5.html.

[79] Sol3a class aaa solar simulators, 2021. URL https://www.newport.com/f/class-aaa-solar-simulators.

[80] *Measuring Photovoltaic Cell I-V Characteristics with the Model 2420 SourceMeter Instrument*. Tektronix, 2013.

[81] Dark iv measurements. URL https://www.pveducation.org/pvcdrom/characterisation/dark-iv-measurements.

[82] Christoph Cobet. *Ellipsometry of Functional Organic Surfaces and Films*, volume 52, chapter 1, pages 1–22. Springer, second edition, 2014.

[83] L. Jan Anton Koster, Sean E. Shaheen, and Jan C. Hummelen. Pathways to a new efficiency regime for organic solar cells. *Advanced Energy Materials*, 2(10):1246–1253, 2012. doi: https://doi.org/10.1002/aenm.201200103. URL https://onlinelibrary.wiley.com/doi/abs/10.1002/aenm.201200103.

[84] *Guide to Using WVASE32*. J. A. Woollam Co., Inc., 2001.

[85] Agilent. Agilent cary 4000/5000/6000i series uv-vis-nir spectrophotometers. PDF, May 2020. URL https://www.agilent.com/cs/library/brochures/5990-7786EN_Cary-4000-5000-6000i-UV-Vis-NIR_Brochure.pdf.

[86] D. F. Swinehart. The beer-lambert law. *Journal of Chemical Education*, 39(7):333, 07 1962. doi: 10.1021/ed039p333. URL https://doi.org/10.1021/ed039p333.

[87] *X-Ray Reflectometry (XRR)*. Rigaku. URL https://www.rigaku.com/techniques/x-ray-reflectometry-xrr.

[88] L. N. Koppel and L. Parobek. Thin-film metrology by rapid x-ray reflectometry. *AIP Conference Proceedings*, 449(1):469–473, 1998. doi: 10.1063/1.56834. URL https://aip.scitation.org/doi/abs/10.1063/1.56834.

[89] L. G. Parratt. Surface studies of solids by total reflection of x-rays. *Phys. Rev.*, 95:359–369, Jul 1954. doi: 10.1103/PhysRev.95.359. URL https://link.aps.org/doi/10.1103/PhysRev.95.359.

[90] Bruker. Dimension icon - atomic force microscope system with scanasyst. PDF, 2013. URL https://pdf.directindustry.com/pdf/bruker-nano-surfaces/dimension-icon-product-brochure/57554-419017.html.

[91] V. D. Mihailetchi, J. Wildeman, and P. W. M. Blom. Space-charge limited photocurrent. *Phys. Rev. Lett.*, 94:126602, Apr 2005. doi: 10.1103/PhysRevLett.94.126602. URL https://link.aps.org/doi/10.1103/PhysRevLett.94.126602.

[92] Meysam Raoufi Le Quang Phuong Oskar J. Sandberg Huilan Guan Yingping Zou Dieter Neher Safa Shoaee Nurlan Tokmoldin, Seyed Mehrdad Hosseini. Extraordinarily long diffusion length in pm6:y6 organic solar cells. 2020.

[93] Jiangquan Mai, Yiqun Xiao, Guodong Zhou, Jiayu Wang, Jingshuai Zhu, Ni Zhao, Xiaowei Zhan, and Xinhui Lu. Hidden structure ordering along backbone of fused-ring electron acceptors enhanced by ternary bulk heterojunction. *Advanced Materials*, 30(34):1802888, 2018. doi: https://doi.org/10.1002/adma.201802888. URL https://onlinelibrary.wiley.com/doi/abs/10.1002/adma.201802888.

List of Acronyms

List of Figures

List of Tables

AMBMAMTCPJAKMLJMFMTCMRMJMRSMVFIPEVCV